Amelioration of Brain Histone Methylopathies by Balancing a Writer-Eraser Duo KMT2A-KDM5C

Christina N. Vallianatos[1], Brynne Raines[2], Robert S. Porter[1], Michael C. Wu[3], Patricia M. Garay[1], Katie M. Collette[2], Young Ah Seo[4], Yali Dou[5], Catherine E. Keegan[1,6], Natalie Tronson[2,*], and Shigeki Iwase[1,*]

[1]Department of Human Genetics, Michigan Medicine, University of Michigan, Ann Arbor, MI 48109

[2]Department of Psychology, College of LS&A, University of Michigan, Ann Arbor, MI 48109

[3]Neurodigitech, LLC, San Diego, CA

[4]Department of Nutritional Sciences, School of Public Health, University of Michigan, Ann Arbor, MI 48109

[5]Department of Pathology, Michigan Medicine, University of Michigan, Ann Arbor, MI 48109

[6]Department of Pediatrics, Michigan Medicine, University of Michigan, Ann Arbor, MI 48109

* Co-corresponding authors

Please address correspondence to: siwase@umich.edu and ntronson@umich.edu

Abstract

Histone H3 lysine 4 methylation (H3K4me) is extensively regulated by seven writer- and six eraser-enzymes in mammals. Nine H3K4me enzymes are associated with neurodevelopmental disorders to date, indicating their important roles in the brain. Opposing activities of writer-eraser enzymes highlight activity modulation as a therapeutic strategy. However, interplay among H3K4me enzymes in the brain remains largely unknown. Here, we show functional interactions of a writer-eraser duo, *KMT2A* and *KDM5C*, which are responsible for Wiedemann-Steiner Syndrome (WDSTS), and mental retardation X-linked syndromic Claes-Jensen type (MRXSCJ), respectively. Despite opposite enzymatic activities, the WDSTS and MRXSCJ mouse models, deficient for either *Kmt2a* or *Kdm5c*, shared similar brain transcriptomes, reduced dendritic spines, and increased aggression. Double mutation of *Kmt2a* and *Kdm5c* partially corrected altered H3K4me landscapes and transcriptomes from each single mutants, and clearly reversed dendritic morphology deficits and key behavioral traits including aggression. Thus, our study uncovers common yet mutually-suppressive aspects of WDSTS and MRXCJ and provides a proof of principle for balancing a single writer-eraser pair to ameliorate their associated disorders.

Introduction

Dysregulation of histone methylation has emerged as a major contributor of neurodevelopmental disorders (NDDs) such as autism spectrum disorder and intellectual disability (1-3). Histone methylation can be placed on a subset of lysines and arginines by histone methyltransferases (writer enzymes) and serves as a signaling platform for a variety of nuclear events including transcription (4). Reader proteins specifically recognize methylated histones, thereby converting methylation signals into higher-order chromatin structures (5). Histone methylation can be removed by a set of histone demethylases (eraser enzymes) (6). All three classes of methyl-histone regulators are heavily mutated in NDDs, indicating critical, yet poorly-understood, roles of histone methylation dynamics in brain development and function (7-9).

Histone H3 lysine 4 methylation (H3K4me) is one of the most well-characterized histone modifications. H3K4me is primarily found at transcriptionally active areas of the genome. The three states, mono-, di-, and tri-methylation (H3K4me1-3), uniquely mark gene regulatory elements and play pivotal roles in distinct steps of transcription. While H3K4me3/2 are enriched at transcriptionally-engaged promoters, H3K4me1 is a hallmark of transcriptional enhancers (10, 11). At promoters, H3K4me3 contributes to recruitment of general transcription machinery TFIID and RNA polymerase II (12, 13). H3K4me1 has been shown to tether BAF, an ATP-dependent chromatin remodeling complex, at enhancers (14).

61 H3K4me is extensively regulated by seven methyltransferases and six demethylases in
62 mammals (6). Consistent with the important roles of H3K4me in transcriptional
63 regulation, genomic distribution of H3K4me appears highly dynamic during brain
64 development (15), in which widespread gene expression changes take place.
65 Developmental H3K4me dynamics appears to be altered in the prefrontal cortices of
66 individuals with autism (16, 17). However, contributions of each of the 13 enzymes in
67 the dynamic H3K4me landscapes of the developing brain remains largely unknown.
68 Strikingly, genetic alterations in nine of the 13 H3K4me enzymes and at least two
69 H3K4me readers have been associated with human NDDs to date, indicating critical
70 roles of H3K4me balance (18) (Figure 1A). These human conditions can be collectively
71 referred to as brain H3K4 methylopathies and point to non-redundant yet poorly-
72 understood roles of these genes controlling this single post-translational modification for
73 faithful brain development.
74
75 As histone modifications are reversible, one can, in theory, correct an imbalance by
76 modulating the writers or erasers. Chemical inhibitors of histone deacetylases (HDACs)
77 have been successfully used to rescue phenotypes in mouse models of NDDs. HDAC
78 inhibitors were able to ameliorate learning disabilities in mouse models of Rubinstein-
79 Taybi and Kabuki syndromes, which are deficient for CREBBP or KMT2D, writer
80 enzymes for histone acetylation or H3K4me, respectively (19, 20). However, none of
81 these chemical compounds has yet been proven applicable to human NDDs. Moreover,
82 the HDAC inhibitors such as SAHA and AR-42 used in these studies interfere with
83 multiple HDACs (21), which could potentially result in widespread side effects. Given

84 the non-redundant roles of the H3K4me enzymes, a more specific perturbation is
85 desirable.
86
87 In order to achieve specific modulation of H3K4me rather than inhibiting multiple histone
88 modifiers in a given NDD, an important first step is to delineate functional relationships
89 between the H3K4 enzymes. In the present work, we focus on a pair of NDD-associated
90 writer/eraser enzymes: KMT2A and KDM5C. Haploinsufficiency of *KMT2A* underlies
91 Weidemann-Steiner Syndrome (WDSTS), characterized by developmental delay,
92 intellectual disability, characteristic facial features, short stature, and hypotonia (22, 23).
93 Loss of KDM5C function defines Mental Retardation, X-linked, syndromic, Claes Jensen
94 type (MRXSCJ), in which individuals display an intellectual disability syndrome with
95 aggression, short stature, and occasional autism comorbidity (24-27). Mouse models
96 have provided experimental support for causative impacts of KMT2A and KDM5C
97 deficiencies in impaired cognitive development. Heterozygous *Kmt2a* knockout (KO)
98 mice show compromised fear learning (28), and excitatory-neuron-specific *Kmt2a*
99 deletion similarly led to impaired learning, memory, and anxiety behaviors, as well as
100 altered H3K4me3 distributions and transcriptomes (29, 30). In these studies, however,
101 the social behavior and relevant cellular consequences of *Kmt2a* loss were not
102 examined. *Kdm5c*-knockout (KO) mice mimic many MRXSCJ features, including small
103 body size, aggressive behavior, and reduced social activity and learning (31, 32).
104 *Kdm5c*-KO neurons in the basolateral amygdala exhibit malformation of dendritic arbors
105 and spines along with misregulation of neurodevelopmental genes. However, the
106 functional relationships between KMT2A and KDM5C, e.g. how deficiencies in opposing

enzymatic activities can lead to same learning deficits, remain completely unknown. Additionally, despite the strong association with NDDs, successful modulation of histone methylation to restore normal brain physiology has not been reported in these or any other animal models of histone methylopathies.

In the present work, we tested whether modulating either single H3K4me writer or eraser can ameliorate the neurodevelopmental symptoms observed in the WDSTS and MRXSCJ mouse models. We generated *Kmt2a*-, *Kdm5c*-double mutant (DM) mice, and performed systematic comparisons between wild-type (WT), single mutants, and DM mice. The results detailed below revealed common yet mutually-suppressive traits in the two disease models, thereby providing a binary therapeutic strategy for the two conditions.

Results

KMT2A and KDM5C co-exist broadly in the brain

We first examined expression patterns of KMT2A and KDM5C using publicly-available resources, and found the two genes are broadly expressed throughout brain regions of adult mice and humans (Figure S1) (33-37) (38). *Kmt2a* and *Kdm5c* are expressed at comparable levels in all major excitatory and inhibitory neuron subtypes as well as glia cells in mouse visual cortex (Figure S1A), and also throughout mouse brains (Figure S1B). Consistently, developing and aging human brains express *KMT2A* and *KDM5C* at high, steady levels (Figure S1C). Thus, both writer and eraser are co-expressed across brain cell types, regions, and developmental stages in both human and mouse.

Generation of *Kmt2a-Kdm5c* double-mutant (DM) mice

To test genetic interaction of *Kmt2a* and *Kdm5c in vivo*, we generated *Kmt2a-Kdm5c* double-mutant (DM) mice. Experimental mice were F1 hybrids of the two fully-congenic laboratory mouse strains: 129S1/SvImJ *Kmt2a*$^{+/-}$ males (39) and C57BL/6J *Kdm5c*$^{+/-}$ females (31) (Figure 1B). This cross resulted in the following genotypes of male mice: wildtype (WT); *Kmt2a* heterozygote (*Kmt2a*-HET: *Kmt2a*$^{+/-}$), *Kdm5c* hemizygous knock-out (*Kdm5c*-KO: *Kdm5c*$^{-/y}$), and *Kmt2a-Kdm5c* double-mutant (DM: *Kmt2a*$^{+/-}$, *Kdm5c*$^{-/y}$), thereby allowing us to perform systematic comparison between the WDSTS model (*Kmt2a*-HET), the MRXSCJ model (*Kdm5c*-KO), and their composite (DM). We focus on males, because MRXSCJ predominantly affects males and *Kdm5c*-heterozygous female mice exhibit only minor cognitive deficits (32).

These mice were born at expected Mendelian ratios of 25% per genotype, demonstrating the DM mice were not synthetic lethal (Figure 1C). Genotypes were confirmed at RNA and DNA levels (Figure S2A-C), and protein level for KDM5C (Figure S2D). Brain anatomy showed no gross deformities in any of the genotypes (Figure S2E). Body weight, during the course of development and in adult, however, was reduced in the two single mutants as well as in DM mice (Figure 1D-E). The weight reduction was slightly more pronounced in DM compared to single mutants ($F(3,82) = 11.76$, $p < 0.001$, One-way ANOVA). Thus, loss of *Kdm5c* and *Kmt2a* heterozygosity both led to growth retardation, which was not corrected but rather slightly exacerbated in DM mice.

Altered H3K4me3 landscapes in WDSTS and MRXSCJ models and rescue effects in DM

H3K4me3 is a reaction product of KMT2A-mediated methylation (40), while a substrate for KDM5C-mediated demethylation (41, 42). We sought to determine the impact of KMT2A- and KDM5C-deficiencies and double mutation on the H3K4me3 landscape within the brain. We chose to examine the amygdala tissue, because it plays crucial roles in social behavior and fear memory, which are impaired in *Kdm5c*-KO mice (31). In Western blot analyses, global H3K4me1-3 levels were not altered dramatically in any mutant (Figure S3A). We thus performed H3K4me3 chromatin immunoprecipitation coupled with deep sequencing (ChIP-seq) to probe local changes genome-wide. To assess the IP specificity, we spiked-in an array of recombinant nucleosomes carrying 15

165 common methylations along with DNA barcodes appended to the Widom601
166 nucleosome positioning sequence (43) (see Methods). The two H3K4me3 nucleosomes
167 dominated the Widom601-containing DNA in all IP reactions with negligible signals from
168 other methylation states such as H3K4me1 or H3K4me2 (Figure S3B), demonstrating a
169 superb specificity of the ChIP.
170
171 To obtain a global picture of H3K4me changes, we examined the H3K4me3 signals
172 between WT and the three mutants throughout the mouse genome partitioned into 1-
173 kilobase (kb) bins (Figure 2A). We found an overall similarity in H3K4me3 coverage
174 across *Kmt2a*-HET, *Kdm5c*-KO, and DM on a genome-wide scale, as well as at
175 promoter regions (Figure 2A, Figure S3C). We then broke down the genome into
176 promoter (± 1 kb from transcription start sites [TSS]), intergenic (between genes), and
177 intragenic (within a gene) regions, and asked if any areas are preferentially
178 dysregulated in any of the mutant animals. In WT, 61% of H3K4me3 fell within
179 promoters, consistent with H3K4me3 as a hallmark of promoters (11-13), while smaller
180 fractions, 18% and 21%, were found in intergenic or intragenic regions, respectively
181 (Figure S3D). This H3K4me3 distribution pattern was largely consistent across the other
182 genotypes (Figure S3D), except for *Kdm5c*-KO and DM amygdala which had slightly
183 higher proportions of intragenic (25% for both) and intergenic (30% and 29%,
184 respectively) methylation (Figure S3D).
185
186 Examining local differentially-methylated regions (DMRs), i.e. either hyper- or hypo-
187 methylated for H3K4me3 compared to WT, we found fewer DMRs in *Kmt2a*-HET

188 (1,940) than in *Kdm5c*-KO (11,990) (Figure 2B-G, Figure S3E-H). This difference is
189 likely due to the heterozygosity of *Kmt2a* which leaves one functional copy of *Kmt2a,*
190 versus the complete loss of *Kdm5c*. Consistently, complete loss of *Kmt2a* in
191 hippocampal neuronal nuclei was previously shown to reduce H3K4me3 in more than
192 four thousand loci (30). In the *Kmt2a*-HET amygdala, hypermethylated loci were
193 primarily found at intragenic regions (56%), while hypomethylated regions were found
194 mainly at promoters (76%, Figure 2C). *Kdm5c*-KO DMRs were biased towards an
195 increase in methylation signals (8,284 hypermethylated vs. 3,706 hypomethylated),
196 consistent with loss of a demethylase. In the *Kdm5c*-KO amygdala, the hypermethylated
197 loci showed a roughly even split between promoters, intragenic, and intergenic regions,
198 while the majority of the *Kdm5c*-KO hypomethylated regions were located at promoters
199 (89%, Figure 2F). Hypermethylation in non-promoter regions was also detected as an
200 appearance of additional H3K4me3 peaks in *Kdm5c*-KO amygdala (Figure S3D). When
201 we overlapped single mutant DMRs (Figure 2H), most DMRs were unique to *Kdm5c*-KO
202 (10,994). Interestingly, one half of the *Kmt2a*-HET DMRs overlapped with *Kdm5c*-DMRs
203 (Figure 2H), and most of these DMRs were largely misregulated in the same direction
204 between the two single mutants (Figure 2I), despite the opposing activity of this pair of
205 enzymes. Motif analysis identified distinct as well as common transcription factor-
206 binding motifs at *Kmt2a*-HET and *Kdm5c*-KO DMRs (Figure SI-J). Thus, *Kmt2a*- and
207 *Kdm5c*-deficiencies lead to both unique and common alterations in H3K4me3
208 landscapes.
209

210 We next asked if any of these DMRs were corrected in double mutants (DM). We
211 defined “rescued” regions as DMRs identified in single mutants that were no longer
212 categorized as a DMR in DM (therefore, no different from WT). We observed a rescue
213 of roughly half of single mutant DMRs in our DM animals: 42% (821/1,940) of *Kmt2a*-
214 HET DMRs and 54% (6,576/11,990) of *Kdm5c*-KO DMRs were not called as
215 differentially methylated in DM (Figures 2D, 2G, S3E-H). Representative examples of
216 rescued and unrescued DMRs are shown (Figure 2J-M).
217
218 Most rescued DMRs show smaller yet detectable fold changes of H3K4me3 in DM,
219 indicating that the rescue effect was partial (Figure 2N). If KMT2A and KDM5C simply
220 counteract, we should observe that hypermethylated regions in *Kdm5c*-KO are
221 hypomethylated in *Kmt2a*-HET, and normalized in DM. We indeed observed such cases
222 in a small fraction of rescued DMRs (solid bars in Figure 2N). Unexpectedly, some
223 regions showed reciprocal H3K4me3 changes between the single mutants in an
224 opposite way as expected; namely, hypomethylation in *Kdm5c*-KO and
225 hypermethylation in *Kmt2a*-HET (open bars in Figure 2N). The most prevalent pattern of
226 rescued DMRs was the hypermethylated regions of *Kdm5c*-KO that were still
227 moderately hypermethylated in DMs and unexpectedly in *Kmt2a*-HET as well (striped
228 bars in Figure 2N). Thus, simple counteractions between *Kmt2a* and *Kdm5c* are
229 relatively rare events, and rather deficiency of the single enzyme results in a complex
230 change of H3K4me3 homeostasis. Nonetheless, our analyses identified thousands of
231 genomic loci at which KMT2A and KDM5C fully or partially mediate aberrant H3K4me3
232 levels caused by loss of the opposing enzyme.

233

234 **Transcriptomic similarity between WDSTS and MRXSCJ models and rescue**

235 **effects in DM**

236 We previously showed *Kdm5c*-KO mice exhibit aberrant gene expression patterns in the
237 amygdala and frontal cortex (31), and the hippocampus (32). Excitatory-neuron specific
238 conditional *Kmt2a*-KO mice were also characterized with altered transcriptomes in the
239 hippocampus and cortex (29, 30). However, the global gene expression of *Kmt2a*-HET,
240 which is akin to the WDSTS syndrome genotypes, has not been determined. To
241 compare the impact of *Kmt2a*-haploinsufficiency and *Kdm5c*-KO on the transcriptome,
242 we performed unique molecular identifiers (UMI)-RNA-seq (44) using amygdala tissues
243 of adult mice across the four genotypes. To minimize the impact of PCR-derived
244 duplication on gene expression analysis, we used primers containing UMIs during
245 library amplification, and deduplicated the sequencing reads prior to analysis (see
246 Methods). First, we confirmed the lack or reduction of reads from *Kdm5c* exons 11 and
247 12 and *Kmt2a* exons 8 and 9 in the corresponding mutants (Figure S2A-B). Spike-in
248 RNA controls confirmed the broad dynamic range of differential gene expression
249 analysis (Figure S4A). The gene expression changes observed in the *Kdm5c*-KO
250 amygdala were similar between the present dataset and our previous dataset obtained
251 from a different cohort of mice (31), demonstrating the reproducibility of the UMI-RNA-
252 seq approach (Figure S4B).

253

254 We identified a similar number of differentially-expressed (DE) genes ($p < 0.01$) in
255 *Kmt2a*-HET (136 genes) and *Kdm5c*-KO (127 genes) compared to WT amygdala, while

256 DM yielded 203 DE genes (Figure 3A). In general, KMT2A acts as a transcriptional
257 coactivator by placing H3K4me (39, 40, 45) and KDM5C primarily suppresses
258 transcription by removing this mark (41), yet roles for KDM5C as a positive regulator of
259 transcription have also been reported (46, 47). Reminiscent of some H3K4me changes
260 that were similar between the single mutants (Figure 2I and 2N), examination of fold
261 changes of all DE genes pointed to similar transcriptome alterations in all three mutants
262 compared to WT (Figure 3B). Furthermore, a substantial number of DE genes overlap
263 among the three mutants and many of them showed changes in the same direction
264 between single mutants (Figures 3C, S4C-D), while no genes were reciprocally
265 misregulated (Figure 3D). Consistently, the single-mutant DE genes were largely
266 misregulated in the same direction as the other single mutant (Figure S4E-F). With
267 respect to the biological implications of the gene misregulation, we did not find any
268 conspicuous alterations of neuronal activity-dependent genes, cell-type specific
269 transcripts, and developmentally-regulated genes in any of the mutant DE genes
270 (Figure S5).
271
272 Next, we sought to test if normal expression of any individual genes was restored in
273 DM. To this end, we counted single-mutant DE genes that had higher *p*-values than a
274 relaxed significance threshold ($p > 0.1$) in DM vs. WT comparison; an indicator of
275 normal expression. We found that 33% (42/127) of *Kdm5c*-KO-DE genes and 56%
276 (76/136) *Kmt2a*-HET-DE genes were expressed normally in DM (highlight in Figure 3E).
277 The rescue effects were visible when we analyzed all single-mutant DE genes as a
278 group (Figure S4D). To better understand how transcriptomic similarity and rescue

279 effect can occur simultaneously, we plotted expression fold changes of the 118 rescued
280 genes (Figure 3F). We observed that rescued genes were differentially dysregulated in
281 single mutants, e.g. upregulated in *Kdm5c*-KO but unchanged in *Kmt2a*-HET (Figure
282 3F). Thus, these results indicate that the largely-separate sets of genes contribute to the
283 overall transcriptome similarity and the rescue effect in DM.
284
285 We then examined the relationship between the H3K4me3 landscape and transcriptome
286 alterations. If H3K4me3 changes drive the gene misregulation in mutants, we should be
287 able to observe a correlation between these two datasets. However, genes with altered
288 promoter-proximal H3K4me3 did not show significant changes in their expression as a
289 group (Figure S6A). While H3K4me3 changes are the direct molecular consequences of
290 KMT2A- and KDM5C-deficiency, the steady-state mRNAs we captured in our RNA-seq
291 approach likely involve indirect and adaptive consequences of loss of these enzyme(s),
292 which can lead to an underwhelming correlation between H3K4me3 and transcriptome
293 data. Indeed, we observed a positive correlation between intergenic H3K4me3 levels
294 and spurious transcripts, which are generated at these regions yet likely unstable,
295 therefore, can reflect transcriptional activity more reliably than steady-state mRNA
296 levels (Figure S6B). Such spurious intergenic transcripts were previously observed in
297 the *Kdm5c*-KO hippocampus (32). We also examined the H3K4me3 coverage at
298 promoter regions of DE genes (Figure S6C). Across the different DE gene categories,
299 H3K4me3 levels did not differ between genotypes, with two exceptions: *Kmt2a*-HET
300 down-regulated and *Kdm5c*-KO up-regulated genes showed the expected changes in
301 median H3K4me3 levels (Figure S6C). The correlation was also evident between

302 expression of rescued genes and H3K4me3 (Figure S6D). Together, these observations
303 indicate that H3K4me3 changes are not sufficient, yet an important contributor, for gene
304 misregulation in single mutants and its correction in DM.
305
306 Gene-annotation enrichment analysis of these 118 rescued genes did not yield
307 statistically-significant enrichment of any functional pathways, however, we were able to
308 separate rescued genes into specific biological pathways that could potentially be
309 restored in DM (Supplementary Table 1). Notably, genes that have established roles in
310 central nervous system development and are genetically associated with
311 neurodevelopmental disorders were among these restored genes in DM. These genes
312 include *Gnao1* (48, 49), *Bcl11b* (50), *Arnt2* (51), *Mkks* (52-55), *Arid1a* (56), *Rora* (57),
313 and *Sez6* (58).
314
315 **Shared dendritic phenotypes in *Kmt2a*-HET and *Kdm5c*-KO were reversed in DM**
316 Altered dendrite morphology is a hallmark of many human neurodevelopmental
317 disorders (NDDs), as well as animal models of NDDs (31, 59-62). We previously found
318 that reduced dendritic length and spine density in basolateral amygdala (BLA) neurons
319 of *Kdm5c*-KO adult male mice (31). Assessment of dendritic morphology in *Kmt2a*-HET
320 has not been reported. We performed comparative dendrite morphometry of pyramidal
321 neurons in the BLA using Golgi staining for the four genotypes (Figure 4). For *Kdm5c*-
322 KO neurons, we recapitulated our previous findings of reduced dendrite lengths (Figure
323 4B) ($F(3,89) = 2.776$; $p = 0.0459$; WT vs. *Kdm5c*-KO: $p = 0.0341$, one-way ANOVA
324 followed by Tukey multiple comparison tests) and lower spine density (Figure 4C)

325 ($F(3,89) = 82.25$; $p < 0.0001$; WT vs. *Kdm5c*-KO: $p = 0.0079$). *Kmt2a*-HET neurons
326 looked remarkably similar to *Kdm5c*-KO (Figure 4A), exhibiting trends of reduction in
327 dendrite length, which was not significantly different than WT, however, was also not
328 different than *Kdm5c*-KO (Figure 4B) (WT vs. *Kmt2a*-HET: $p = 0.1772$; *Kdm5c*-KO vs.
329 *Kmt2a*-HET $p = 0.8906$). Similarly, spine densities of *Kmt2a*-HET neurons were
330 significantly lower compared to WT and not significantly different than *Kdm5c*-KO
331 (Figure 4C) (WT vs. *Kmt2a*-HET: $p = 0.0053$; *Kdm5c*-KO vs. *Kmt2a*-HET $p = 0.9993$).
332 Loss of both *Kmt2a* and *Kdm5c* together had an overall positive effect on neuron
333 morphology (Figure 4A). DM dendrite lengths showed trends of restoration (Figure 4B),
334 as they were not significantly different than WT (WT vs. DM: $p = 0.5503$), however were
335 also not different than *Kdm5c*-KO (*Kdm5c*-KO vs. DM: $p = 0.5341$). DM exhibited an
336 increase in dendritic spine density that surpassed a rescue effect (Figure 4C) (WT vs.
337 DM: $p < 0.0001$; *Kdm5c*-KO vs. DM: $p < 0.0001$, *Kmt2a*-HET vs. DM: $p < 0.0001$). As
338 morphology of dendritic spines progressively changes during synaptogenesis and
339 development (63) (Figure S7), we also asked whether developmental subtypes of
340 dendritic spines were altered in any genotype. We did not find dramatic changes in
341 spine morphology among the four genotypes (Figure 4D), indicating selective
342 requirement of *Kdm5c* and *Kmt2a* for regulation of spine numbers, but not for
343 morphology. Overall, we conclude that *Kmt2a*-HET and *Kdm5c*-KO share similar
344 dendritic morphology deficits, which are reversed in DM.
345
346 **Memory alterations in *Kdm5c*-KO were reversed in DM**

347 After observing the restorative molecular and cellular effects in DM mice, we next
348 sought to determine the effect of loss of *Kmt2a* and/or *Kdm5c* on mouse behaviors
349 through a battery of behavioral tests. In accordance with previous findings (31, 32),
350 *Kdm5c*-KO mice showed significant deficits in associative fear memory, as measured by
351 the contextual fear conditioning (CFC) tests (Figure 5A) ($F(3,64) = 2.83$, $p = 0.046$; WT
352 vs. *Kdm5c*-KO: $p = 0.018$). In the novel object recognition tests (NOR), where WT mice
353 showed preference for the new object, *Kdm5c*-KO mice tended to avoid the novel object
354 (Figure 5B) ($F(3,64) = 3.20$, $p = 0.030$; WT vs. *Kdm5c*-KO: $p = 0.007$). Homozygous
355 deletion of *Kmt2a* in excitatory hippocampal neurons leads to impaired fear memory in
356 the CFC (30), a hippocampal-dependent memory test (64). In our tests, *Kmt2a*-HET
357 mice showed no deficits compared to WT mice (Figure 5A-B) (CFC: $p = 0.789$; NOR; p
358 $= 0.888$), indicating stronger cognitive deficits in the MRXSCJ model compared to
359 WDSTS model mice. Importantly, DM mice also showed no differences from WT mice
360 (Figure 5A-B) (CFC: $p = 0.246$; NOR: $p = 0.756$), suggesting that *Kmt2a* heterozygosity
361 can rescue memory deficits of *Kdm5c*-KO mice. These differences in memory tasks
362 were not attributable to differences in locomotor activity or shock responsiveness, as
363 none of these parameters showed significant differences among the genotypes (Figure
364 5C-D).
365

366 **Social behaviors are differently dysregulated in *Kmt2a*-HET, *Kdm5c*-KO, and DM**
367 **mice**

368 In the three-chambered social interaction test (Figure 6A), we observed significant
369 differences between genotypes ($F(3,61) = 4.314$, $p < 0.008$). *Kmt2a*-HET mice showed

370 no differences from WT (p = 0.082), in accordance with previous tests in conditional
371 *Kmt2a*-KO mice (30). In contrast, *Kdm5c*-KO (p= 0.002), as previously shown (31), as
372 well as DM (p = 0.011) mice showed significantly less preference for the stranger
373 mouse compared with WT animals. These data suggest that *Kmt2a* heterozygosity does
374 not rescue deficits of social interaction in the *Kdm5c*-KO.
375
376 In tests of social dominance (Figure 6B), *Kmt2a*-HET mice won against WTs in 60.9% in
377 of the matches against WT (p = 0.091), and *Kdm5c*-KO mice won at least 68.4% of the
378 time (p = 0.008). Surprisingly, DM animals lost more than 80% of their bouts against WT
379 ($p = 1.47 \times 10^{-5}$). Although DM mice were slightly smaller compared to single mutants
380 (Figure 1D), this is unlikely to drive submissive behaviors, as body mass has been
381 shown to have minimal impact on social hierarchy unless excess difference (> 30%) is
382 present between animals (65-67), which is not the case in our study (Figure 1D) (11%
383 *Kmt2a*-HET vs. WT, 17% *Kdm5c*-KO vs. WT, 25% DM vs. WT). These results
384 demonstrate that a significant increase of social dominance in *Kdm5c*-KO and a similar
385 trend in *Kmt2a*-HET are mediated by opposing enzymes.
386
387 In the resident-intruder test, we observed differences in overall aggression between
388 genotypes (Figure 6C) ($F(4,61) = 3.015$, p = 0.037), and differences across specific
389 types of aggressive behaviors (Figures 6D-H, S8A-E) ($F(12,61) = 2.15$, p = 0.015).
390 Specifically, we found increased darting (Figures 6D, S8A) in both *Kdm5c*-KO (p =
391 0.006) and *Kmt2a*-HET (p = 0.032) mice together with decreased aggression in DM
392 mice, which showed significantly less mounting (Figures 6E, S8B) (*cf* WT: p =0.072; *cf*

393 *Kdm5c*-KO: p = 0.019; *cf Kmt2a*-HET: p = 0.004), and chasing (Figures 6F, S8C) (*cf*
394 WT: p =0.027; *cf Kdm5c*-KO: p = 0.010; *cf Kmt2a*-HET: p = 0.007) than all other
395 genotypes. Moreover, we also observed an overall effect of genotype on submissive
396 behaviors of resident mice (Figure 6I) ($F(3,61) = 4.071$, p = 0.011). For the specific type
397 of submissive behaviors, DM mice exhibited significantly more cowering (Figures 6J,
398 S8F) compared with all other genotypes (*cf* WT : p = 0.028; cf *Kdm5c*-KO: p = 0.006; cf
399 *Kmt2a*-HET: p = 0.005), and significantly more running away (Figures 6K, S8G)
400 compared with *Kdm5c*-KO (p = 0.008). Importantly, the genotype effect on submissive
401 behaviors inversely correlated with that of aggressive behavior, reinforcing the
402 difference in specific behaviors rather than changes in locomotor activity.
403
404 Together, the behavioral studies revealed more pronounced deficits of *Kdm5c*-KO
405 animals compared to *Kmt2a*-HET mice on memory and social interaction, while *Kmt2a*-
406 HET and *Kdm5c*-KO mice shared increased social dominance and aggression. The
407 consequences of double mutations varied between the tests, with clear rescue effects
408 on cognitive tasks, dominant behavior, and aggression, and no effect on social
409 interactions. Notably, however, no behavioral traits were exacerbated in DM. These
410 results support the idea that the two enzymes mediate some, if not all, deficiencies
411 caused by writer-eraser imbalance at the behavioral level.

412 **Discussion**

413

414 The present work represents the first genetic interactions between chromatin
415 modification writer and eraser enzymes *in vivo*, to our knowledge. Discovery of
416 chromatin-modifying enzymes in the past decades made it clear that virtually no DNA-
417 or histone-modifications are irreversible, and instead are subjected to dynamic
418 regulation by writer and eraser enzymes. The genes encoding these enzymes appear to
419 have undergone duplication events during evolution. Complex organisms carry a
420 greater number of genes that encode enzymes for single chromatin modification. For
421 example, only one enzyme, Set1, is responsible for H3K4 methylation in fission yeast.
422 In fly, three genes, *Trx*, *Trr*, and *Set1* mediate H3K4me installation, and all three genes
423 were duplicated in the mammalian genomes, which resulted in six SET-family H3K4
424 writers (68). A plethora of work has demonstrated specialized as well as redundant
425 roles of individual histone-modifying enzymes within a family, in broad biological
426 processes such as cancer and development (69). A fundamental question remained —
427 is there any specific writer-eraser pairing in such highly-duplicated gene families for a
428 single chromatin modification? Mishra *et al*. showed that KDM5A antagonizes KMT2A,
429 KMT2B, and KMT2D to modulate the transient site-specific DNA copy number gains in
430 immortalized human cells (70). Cao et al. found that failed differentiation of mouse
431 embryonic stem cells due to *Kmt2d* deletion can be rescued by *Kdm1a* knockdown (71).
432 These pioneering efforts identified functional interplay between the opposing enzymes
433 *in vitro*, however, no *in vivo* study has been reported. Thus, the present study

434 substantially advances our understanding of how methyl-histone writer and eraser
435 enzymes functionally interact during brain development and function.
436
437 Brain development is particularly relevant to the H3K4me dynamics, because a cohort
438 of neurodevelopmental disorders have been genetically associated with impaired
439 functions of these enzymes, as discussed earlier. Our work illuminates the similarities
440 between WDSTS and MRXSCJ model mice in gene expression and neuronal
441 morphological levels, although the two conditions are associated with opposing
442 enzymatic activities. Consistently, many symptoms are common between WDSTS and
443 MRXSCJ, including intellectual disability, short stature, seizures, and aggressive
444 behavior (23-25, 72). Thus, our work underscores a shared pathophysiology of the two
445 conditions. Unlike previous studies using chemical approaches that block multiple
446 chromatin regulators (19-21), we demonstrated that manipulation of a single enzyme,
447 KMT2A or KDM5C, is sufficient to reverse many neurological traits. It may not be
448 surprising that not all traits were reversed in DM mice, such as H3K4me3 at specific loci
449 (Figure 2), expression of some genes (Figure 3), and social preference (Figure 6),
450 because compensatory actions by remaining H3K4me-regulators may potentially
451 mediate these un-rescued traits. Our work opens a new avenue for future studies to
452 delineate the full interplay between the 13 H3K4me-regulatory enzymes throughout
453 brain development and function.
454
455 Increased social dominance is a novel behavioral trait we found in both WDSTS and
456 MRXSCJ mouse models. The amygdala is well known to mediate social behaviors (73,

457 74). For example, lesions of BLA result in decreased aggression-like behavior and
458 increased social interactions (75, 76), and changes in transcriptional regulation in BLA
459 are observed after social interactions (74). Decreased dendritic spine density in *Kmt2a*-
460 HET and *Kdm5c*-KO mice inversely correlates with increased social dominance and
461 aggression (Figures 4 and 6), suggesting that decreased spine density does not
462 represent a loss-of-function in the amygdala, and rather, may reflect a loss of inhibitory
463 control over the amygdala. Thus, determining the connectivity of amygdala with other
464 regions, including prelimbic, infralimbic, and orbitofrontal cortices (77) as well as ventral
465 hippocampus (73) will be critical for understanding the changes in social behaviors in
466 both WDSTS and MRXSCJ models.
467
468 With any therapeutic intervention, careful assessments of side effects will be inevitable.
469 In our work, while a substantial fraction of H3K4me3 DMRs and gene misregulation in
470 single mutants were corrected in DM (Figures 2 and 3), combinatorial ablation of
471 KMT2A and KDM5C should reduce net regulatory action over H3K4me3, which may
472 lead to adverse consequences. Indeed, our genomics approaches identified H3K4me3
473 DMRs that are unique to the DM brain, and several genes uniquely altered in DM
474 animals (Figure S9). It is still plausible that these gene and H3K4me3 changes in DM
475 can lead to phenotypic outcomes that were not examined in this study. Nevertheless,
476 we were encouraged that none of the neurological traits measured in this study showed
477 exacerbation in DM.
478

479 It is important to note that the double mutations introduced in our mice were constitutive,
480 and therefore a lifetime of adaptation to loss of these two major chromatin regulators
481 may occur from early developmental stages. A more realistic therapeutic strategy may
482 be acute inhibition of KDM5C and KMT2A in juvenile or mature brain. Previous work
483 characterizing mouse models with excitatory-neuron specific ablation of *Kdm5c* or
484 *Kmt2a* via *CamKII*-Cre found that conditional *Kmt2a* deletion led to clear learning
485 deficits (30), while cognitive impairments in the conditional *Kdm5c*-KO mice were much
486 milder than those of constitutive *Kdm5c*-KO mice (32). These results suggest a
487 developmental origin of phenotypes in *Kdm5c*-KO. Future investigations are needed to
488 address whether the effects of acute inhibition of opposing enzymes in these mouse
489 models can restore such neurodevelopmental deficits.

490 **Materials & Methods**

491

492 *Mouse models*

493 *Kdm5c*-KO mice were previously described (31). *Kmt2a*-HET mice were generated by
494 crossing previously-described *Kmt2a*-flox (exons 8 and 9) mice with B6.129-
495 Gt(ROSA)26Sor$^{tm1(cre/ERT2)Tyj}$/J-Cre mice (78). To backcross *Kmt2a*$^{+/-}$ mice onto the
496 desired 129S1/SvImJ strain, we employed the marker assisted accelerated
497 backcrossing through Charles River Labs. *Kmt2a*$^{+/-}$ mice were bred to the N4 generation
498 at minimum, where mice were >90% congenic for 129S1/SvImJ. All experimental mice
499 were generated as F1 generation hybrids from mating between 129S1/SvImJ *Kmt2a*$^{+/-}$
500 males and C57Bl/6 *Kdm5c*$^{+/-}$ females: WT males (*Kmt2a*$^{+/+}$*, Kdm5c*$^{+/y}$); *Kdm5c*-KO
501 males (*Kmt2a*$^{+/+}$*, Kdm5c*$^{-/y}$); *Kmt2a*-HET males (*Kmt2a*$^{+/-}$*, Kdm5c*$^{+/y}$); and *Kdm5c-Kmt2a*-
502 DM males (*Kmt2a*$^{+/-}$*, Kdm5c*$^{-/y}$). Genotypes were confirmed using the following primers:
503 for *Kmt2a*, 5'-GCCAGTCAGTCCGAAAGTAC, 5'-AGGATGTTCAAAGTGCCTGC, 5'-
504 GCTCTAGAACTAGTGGATCCC; for *Kdm5c*, 5'-
505 CAGGTGGCTTACTGTGACATTGATG, 5'-TGGGTTTGAGGGATACTTTAGG, 5'-
506 GGTTCTCAACACTCACATAGTG.

507

508 *Western blot analysis*

509 Total proteins from adult brain tissues were subjected to Western blot analysis using in-
510 house anti-KDM5C (31), and anti-GAPDH antibodies (G-9, Santa Cruz). For histone
511 proteins, nuclei were enriched from the dounce-homogenized brain tissues using Nuclei
512 EZ prep Kit (Sigma, NUC-101). DNA were digested with micrococcal nuclease (MNase,

513 NEB) for 10 minutes at room temperature and total nuclear proteins were extracted by
514 boiling the samples with the SDS-PAGE sample buffer. The following antibodies were
515 used for Western blot analyses: anti-H3K4me3 (Abcam, ab8580), anti-H3K4me2
516 (Thermo, #710796), anti-H3K4me1 (Abcam, ab8895), and anti-H3 C-terminus (Millipore,
517 CS204377).
518
519 *Brain histology*
520 Mice were subjected to transcardial perfusion according to standard procedures. Fixed
521 brains were sliced on a freeze microtome, yielding 30 μm sections that were then fixed,
522 permeabilized, blocked, and stained with DAPI. Slides were imaged on an Olympus
523 SZX16 microscope, with an Olympus U-HGLGPS fluorescence source and Q Imaging
524 Retiga 6000 camera. Images were captured using Q-Capture Pro 7 software. Data were
525 collected in a blind fashion, where samples were coded and genotypes only revealed
526 after data collection was complete.
527
528 *ChIP-seq*
529 Brains from adult (6-8 months) male mice were microdissected to enrich for the
530 amygdala. N=2 animals were used for WT, and N=3 animals were used for *Kmt2a*-HET,
531 *Kdm5c*-KO, and DM as biological replicates. Nuclei were isolated using Nuclei EZ prep
532 Kit (Sigma, NUC-101), and counted after Trypan blue staining. 20,000 nuclei for each
533 replicate were subjected to MNase digestion as previously described (79). We
534 essentially followed the native ChIP-seq protocol (79) with two modifications. One was
535 to use a kit to generate sequencing libraries in one-tube reactions (NEB, E7103S).

536 Another modification was to spike-in the panel of synthetic nucleosomes carrying major
537 histone methylations (EpiCypher, SKU: 19-1001) (43). For ChIP, we used the rabbit
538 monoclonal H3K4me3 antibody (Thermo, clone #RM340).
539
540 Libraries were sequenced on the Illumina NextSeq 500 platform, with single-end 75
541 base-pair sequencing, according to standard procedures. We obtained 20 to 59 million
542 reads per sample. Reads were aligned to the mm10 mouse genome (Gencode) and a
543 custom genome containing the sequences from our standardized, synthetic
544 nucleosomes (EpiCypher) for normalization (80), using Bowtie allowing up to 2
545 mismatches. Only uniquely-mapped reads were used for analysis. Range of uniquely
546 mapped reads for input samples was 38-44 million reads. All IP replicates had a mean
547 of 9.1 million uniquely mapping reads (range: 7.4 to 13.9 million). The enrichment of
548 mapped synthetic spike-in nucleosomes compared to input was calculated and used as
549 a normalization coefficient for read depth each ChIP-seq replicate (80).
550
551 Peaks were called using MACS2 software (v 2.1.0.20140616) (81) using input BAM files
552 for normalization, with filters for a q-value < 0.1 and a fold enrichment greater than 1.
553 Differentially-methylated regions (DMRs) were called using the MACS2 bdgdiff
554 command with default parameters and incorporating the synthetic nucleosome
555 normalization into the read depth factor. Bedtools was used to calculate coverage
556 across individual replicates. We also used Bedtools to intersect peaks of interest with
557 mm10 promoters (defined here as ±1 kb from annotated transcription start site [TSS]),
558 intragenic regions (as defined by annotated mm10 gene bodies, but excluding the

559 previously defined promoter region), and intergenic regions (regions that did not overlap
560 with promoters or gene bodies). DMRs from single mutants (2a-HET or 5c-KO) were
561 considered "rescued" in DM animals if that single-mutant peak was *not* called as a DMR
562 in the DM analysis. For the global H3K4me3 analysis, the Bedtools multicov command
563 was used to calculate coverage over 1 kb windows throughout the genome, as well as
564 at each promoter (±1 kb from annotated TSS). HOMER (v4.10) was used to carry out
565 motif enrichment analysis (82). We selected the top 5 motifs, and only motifs from
566 known mammalian ChIP-seq experiments were represented in our data. Normalized
567 bam files were converted to bigwigs for visualization in the UCSC genome browser.
568 Genes near peaks were identified by Bedtools and RefSeq genomic accession number
569 were converted to official gene symbol using bioDBnet (83).
570
571 The ChIP-seq data have been deposited in NCBI's Gene Expression Omnibus (84).
572 Data are accessible through GEO series accession numbers: SuperSeries GSE127818,
573 SubSeries GSE127817, and can be accessed with secure token *ovuhykuazryxrad*.
574
575
576 *RNA-seq*
577 Brains from adult (3 to 6 months) male mice were microdissected to enrich for the
578 amygdala. N=3 animals were used per genotype. Tissue was homogenized in Tri
579 Reagent (Sigma). Samples were subjected to total RNA isolation, and RNA was purified
580 using RNEasy Mini Kit (Qiagen). ERCC spike-in RNA was added at this stage,
581 according to manufacturer's instructions (Life Technologies). Ribosomal RNA was

582 depleted using NEBNext rRNA Depletion kit (New England Biolabs). Libraries were
583 prepared using the Click-seq method, using primers containing unique molecular
584 identifiers (UMIs), as described previously (44). Multiplexed libraries were pooled in
585 approximately equimolar ratios and purified using Agencourt RNAClean XP beads
586 (Beckman Coulter).
587
588 Libraries were sequenced on the Illumina HiSeq 4000 platform, with paired-end 150
589 base pair reads, according to standard procedures. Reads were mapped to the mm10
590 mouse genome (Gencode) using STAR (v2.5.3a) (85), where only uniquely mapped
591 reads were used for downstream analyses. Duplicates were removed using UMI-tools
592 (v0.5.4) (86), and a counts file was generated using FeatureCounts (Subread v1.5.0)
593 (87). BAM files were converted to bigwigs using deeptools (v3.1.3) (88, 89).
594 Differentially expressed (DE) genes were called using DESeq2 (v1.14.1) (90, 91).
595 According to the previous RNA-seq study of *Kdm5c*-KO mice (31), we used $p < 0.01$ to
596 identify DE genes. Data analyses were performed with RStudio (v1.0.136) or GraphPad
597 Prism (v7.00 or 8.02) for Mac (GrapPad Software, La Jolla California USA,
598 www.graphpad.com). Fold change heatmaps was created using shinyheatmap on the
599 web (92). Cell type expression data was downloaded from the Barres lab Brain RNA-
600 seq Portal (93). Cell type enriched genes were determined as having > 5 FPKM in cell
601 type A and > 2 FPKM cell A FPKM/each other cell type FPKM. We identified 471
602 astrocyte (A), 629 neuron (N), 840 micorglia (M), 197 oligodendrocyte precursor (Op),
603 74 newly formed oligodendrocyte (On), 96 myelinating oligodendrocyte (Om), and 716

604 endothelial (E) cell enriched genes. Temporal expression data from human male
605 amygdala was downloaded from the BrainSpan Atlas of Developing Human Brain (94).
606
607 The RNA-seq data have been deposited in NCBI's Gene Expression Omnibus (84).
608 Data are accessible through GEO series accession numbers: SuperSeries GSE127818,
609 SubSeries GSE127722, and can be accessed with secure token *ovuhykuazryxrad*.
610
611 *Neuronal Golgi staining and morphological analyses*
612 Brains from adult (2-8 months) mice were dissected, and brains were incubated in a
613 modified Golgi-Cox solution for 2 weeks at room temperature. The remaining procedure
614 of Golgi immersion, cryosectioning, staining and coverslipping was performed as
615 described previously (95).
616
617 Morphological analyses of dendrites were carried out as described previously (95). Four
618 animals were used for each genotype, and pyramidal neurons in the basolateral
619 amygdala per animal were quantified: N=24 neurons for WT, *Kmt2a*-HET and *Kdm5c*-
620 KO and N=27 neurons for DM. Quantification was done using commercially available
621 software, NeuroLucida (v10, Microbrightfield, VT), installed on a Dell PC workstation
622 that controlled Zeiss Axioplan microscope with a CCD camera (1600 x 1200 pixels) and
623 with a motorized X, Y, and Z-focus for high-resolution image acquisition (100X oil
624 immersion) and quantifications. The morphological analyses included: dendritic lengths,
625 spine counts, and spine subtype morphology. All sample genotypes were blinded to the
626 analysts throughout the course of the analysis.

627

628 The criteria for selecting candidate neurons for analysis were based on: (1) visualization
629 of a completely filled soma with no overlap of neighboring soma and completely filled
630 dendrites, (2) the tapering of most distal dendrites; and (3) the visualization of the
631 complete 3-D profile of dendritic trees using the 3-D display of the imaging software.
632
633 For quantitative analysis of spine subtypes (thin, stubby, mushroom, filopodia and
634 branched spines), only spines orthogonal to the dendritic shaft were included in this
635 analysis, whereas spines protruding above or beneath the dendritic shaft were not
636 sampled. This principle remained consistent throughout the course of analysis.
637
638 After completion, the digital profile of neuron morphology was extrapolated and
639 transported to a multi-panel computer workstation, then quantitated using
640 NeuroExplorer program (Microbrightfield, VT), followed by statistical analysis (one- and
641 two-way ANOVAs, $p < 0.05$).
642
643 *Behavioral paradigms*
644 Prior to behavioral testing, mice were acclimated to the animal colony room for one
645 week single-housing in standard cages provided with lab diet and water *ad libitum*. A
646 12-hour light-dark cycle (7:00AM-7:00PM) was utilized with temperature and humidity
647 maintained at 20 ±2 ºC and >30%, respectively. The University of Michigan Committee
648 on the Use and Care of Animals approved all tests performed in this research. Five
649 tests, listed in order of testing, were performed: Novel Object Recognition (5 days),

650 Context Fear Conditioning (2 days), Three-Chambered Social Interaction (2 days),
651 Social Dominance Tube Test (3-4 days), and Resident-intruder (2-3 days). All testing
652 was conducted in the morning by experimenters blind to genotype. 70% ethanol was
653 used as a cleaning agent in every test between each trial. Data were collected in a blind
654 fashion, where mice were coded and genotypes only revealed after testing was
655 complete.
656
657 *Novel Object Recognition:* Mice were first habituated to testing arenas (40 x 30 x 32.5
658 cm^3) in three, 10 minute sessions over six consecutive days (96, 97). 24 hours later,
659 mice were allowed to explore on two identical objects (jar or egg, counterbalanced
660 across animals) for two, 10-minute trials spaced three hours apart. All animals were
661 returned to the arena tested 24 hours after the first training session and presented with
662 one training object ("familiar" object: jar or egg) and one "novel" object (egg or jar).
663 Exploration of the objects was defined as nose-point (sniffing) within 2 cm of the object.
664 Behavior was automatically measured by Ethovision XT9 software using a Euresys
665 Picolo U4H.264No/0 camera (Noldus, Cincinnati, OH). Preference was calculated as
666 the time spent exploring novel object/total time exploring both objects. One-sample t-
667 tests against 50% (no preference) were used to establish whether animals remembered
668 the original objects.
669
670 *Contextual Fear Conditioning:* Context fear conditioning was assessed as previously
671 described (98). Mice were placed into a distinct context with white walls (9 ¾ × 12 ¾ × 9
672 ¾ in) and a 36 steel rod grid floor (1/8 in diameter; ¼ spaced apart) (Med-Associates,

673 St. Albans, VT) and allowed to explore for 3 minutes, followed by a 2-second 0.8 mA
674 shock, after which mice were immediately returned to their home cages in the colony
675 room. 24 hours later, mice were returned to the context and freezing behavior was
676 assessed with NIR camera (VID-CAM-MONO-2A) and VideoFreeze (MedAssociates, St
677 Albans, VT). Freezing levels were compared between genotypes using a between-
678 groups analysis (one-way ANOVA) with genotype as the between-subjects factor.
679
680 *Three-Chambered Social Interaction:* Mice were placed into a three-chambered
681 apparatus consisting of one central chamber (24 x 20 x 30 cm^3) and two identical side
682 chambers (24.5 x 20 x 30 cm^3) each with a containment enclosure (8 cm diameter; 18
683 cm height; grey stainless steel grid 3 mm diameter spaced 7.4 mm apart) and allowed
684 to habituate for 10 minutes. 24 hours later, mice were returned to the apparatus that
685 now included a 2-3 month old stranger male mouse (C57BL/6N) on one side of the box
686 ("stranger"), and a toy mouse approximately same size and color as stranger mouse on
687 other ("toy"). Exploration of either the stranger or toy was defined as nose-point
688 (sniffing) within 2 cm of the enclosure and used as a measure of social interaction (99).
689 Behavior was automatically scored by Ethovision XT9 software as described above, and
690 social preference was defined as time exploring stranger/total exploration time. Social
691 preference was analyzed using one-sample t-tests for each genotype. A repeated
692 measures analysis was used for each aggression (genotype x aggression measures
693 ANOVA) and submissive behaviors (genotype x submissive) to analyze aggressive
694 behaviors.
695

696 *Social Dominance Tube Test:* 24 hours prior to testing, mice were habituated to the
697 plastic clear cylindrical tube (1.5 in diameter; 50 cm length) for 10 minutes. During test,
698 two mice of different genotypes were placed at opposite ends of the tube and allowed to
699 walk to the middle. The match concluded when the one mouse (the dominant mouse)
700 forced the other mouse (the submissive mouse) to retreat with all four paws outside of
701 the tube (a "win" for the dominant mouse) (100-102). Each mouse underwent a total of
702 three matches against three different opponents for counterbalancing. Videos were
703 recorded by Ethovision XT9 software as described above, and videos were manually
704 scored by trained experimenters blind to genotype. The number of "wins" was reported
705 as a percentage of total number of matches. Data were analyzed using an Exact
706 Binomial Test with 0.5 as the probability of success (win or loss).
707
708 *Resident-intruder aggression:* Resident-intruder tests were used to assess aggression.
709 Tests performed on consecutive days, where the resident mouse was exposed to an
710 unfamiliar intruder mouse for 15 minutes (103, 104). A trial was terminated prematurely
711 if blood was drawn, if an attack lasted continuously for 30 seconds, or if an intruder
712 showed visible signs of injury after an attack. Resident mice were assessed for active
713 aggression (darting, mounting, chasing/following, tail rattling, and boxing/parrying), as
714 well as submissive behaviors (cowering, upright, running away). Intruder mice were
715 assessed for passive defense (freezing, cowering, and digging). Behavior was recorded
716 and videos scored manually by experimenters blind to genotype. Data were analyzed
717 using a between groups analysis (one-way ANOVA) with genotype as the between-
718 subjects factor.

Acknowledgements

We thank Dr. Ken Kwan, Mandy Lam, and Own Funk for their assistance with the Click-seq library preparation protocol and use of their microscope; Chris Gates for his assistance with RNA-seq analyses; and Clara Farrehi, Jordan Rich, and Demetri Tsirukis for their assistance with experiments for transcriptome analyses, global histone methylation Western blots, and brain histology, respectively. We also thank Drs. Sally Camper, Kenneth Kwan, Stephen Parker, Stephanie Bielas, Michael-Christopher Keogh, as well as the members of the Iwase and Bielas labs, for helpful discussions and critical review of the data.

Conflict of Interest

MCW is CEO of Neurodigitech, LLC. The other authors declare no conflict of interest.

Author Contributions

CNV, NT, and SI conceived the study and designed the experiments. YAS performed global H3K4me3 analyses. RSP performed H3K4me3 ChIP-seq analyses. PMG analyzed RNA-seq data for activity-dependent genes. MCW oversaw dendritic morphometry analyses. BR and KMC performed the mouse behavioral tests under the guidance of NT. CNV performed all other experiments and analyses. YD and CEK provided key experimental recourse and made important intellectual contributions. All authors contributed to the writing and editing of the manuscript.

Funding

This work was funded by an NIH National Research Service Award T32-GM07544 (University of Michigan Predoctoral Genetics Training Program) from the National Institute of General Medicine Sciences (to CNV), an NIH National Research Service Award T32-HD079342 (University of Michigan Predoctoral Career Training in the Reproductive Sciences Program) from the National Institute of Child Health and Human Development (NICHD) (to CNV), University of Michigan Rackham Predoctoral Research Grants (to CNV), a Michigan Institute for Clinical and Health Research fellowship (Translational Research Education Certificate, supported by UL1TR000433 and UL1TR002240) (to CNV), a University of Michigan Rackham Predoctoral Fellowship award (to CNV), an Autism Science Foundation Predoctoral Fellowship award (to CNV), an NIH National Research Service Award F31NS103377 from the National Institute of Neurological Disease & Stroke (NINDS) (to RSP), NIH NINDS Awards (R01NS089896 and R21NS104774) (to SI), Basil O'Connor Starter Scholar Research Awards from March of Dimes Foundation (to SI), and a Farrehi Family Foundation Grant (to SI).

757 **Figure Legends**

758

759 **Figure 1. The H3K4 methylopathies and generation of the *Kmt2a-Kdm5c* double-**
760 **mutant (DM) mouse. (A)** Histone H3 lysine 4 (H3K4me) methyltransferases (writers)
761 and demethylases (erasers) depicted by their ability to place or remove H3K4me.
762 Reader proteins recognizing specific H3K4me substrates (arrows) are depicted below.
763 Genes are listed next to their associated neurodevelopmental disorder. KMT2A and
764 KDM5C are highlighted in purple and green, respectively. WDSTS: Weideman-Steiner
765 Syndrome; ID: intellectual disability; ASD: autism spectrum disorder, CPRF: cleft palate,
766 psychomotor retardation, and distinctive facial features; ARID: autosomal recessive ID;
767 MRXSCJ: mental retardation, X-linked, syndromic, Claes-Jensen type. **(B)** Mouse
768 breeding scheme crossing congenic 129S1/SvlmJ *Kmt2a*-heterozygous males with
769 congenic C57/Bl6 *Kdm5c*-heterozygous females, resulting in F1 generation mice. Only
770 males were used in this study. **(C)** Numbers of male offspring across 30 litters, showing
771 Mendelian ratios of expected genotypes. **(D)** Left panel: Body weight of adult mice > 2
772 months of age (mean ± SEM, ****$p < 0.0001$ in One-way ANOVA). Right panel:
773 Difference between group means of weight (mean ± 95% confidence intervals, *$p<0.05$,
774 **$p<0.01$, ***$p<0.001$, ****$p<0.0001$ in Tukey multiple comparison test). **(E)** Body weight
775 tracked from birth, postnatal day 1 (P1).

776

777 **Figure 2. Altered H3K4me3 landscapes in the amygdala and rescue effect in DM.**
778 **(A)** H3K4me3 coverage in 2a-HET, 5c-KO, or DM compared to WT across the genome,
779 that was partitioned into 1 kilobase (kb) bins. **(B-D)** *Kmt2a*-HET differentially-methylated

780 regions (DMRs), identified as peaks hypermethylated or hypomethylated compared to
781 WT using MACS2 (81) (q < 0.1) **(B)**, their location at promoters, within genes
782 (intragenic), or between genes (intergenic) **(C)**, and how many were rescued in DM **(D)**.
783 **(E-G)** *Kdm5c*-KO DMRs, identified as peaks hypermethylated or depleted compared to
784 WT **(E)**, their location at promoters, within genes (intragenic), or between genes
785 (intergenic) **(F)**, and how many were rescued in DM **(G)**. **(H)** Overlap between all
786 *Kdm5c*-KO and *Kmt2a*-HET DMRs. **(I)** Heatmap of H3K4me3 fold change relative to
787 WT, of 996 shared DMRs between *Kmt2a*-HET and *Kdm5c*-KO. Scale indicates log2
788 fold change of depleted (blue) to enriched (yellow) H3K4me3. **(J-M)** Peak track view of
789 two representative loci for each of the major genome areas: promoter **(J)**, intragenic **(K)**,
790 and intergenic **(L)** DMRs rescued in DM, or un-rescued in DM **(M)**. **(N)** Heatmap of
791 H3K4me3 fold change relative to WT, of 7,397 rescued DMRs. Side bars indicate
792 patterns of rescued regions: solid bars = hypermethylated in 5c-KO, hypomethylated in
793 *Kmt2a*-HET; open bars = hypermethylated in both *Kdm5c*-KO, and *Kmt2a*-HET; dashed
794 bars = hypermethylated in all *Kdm5c*-KO, *Kmt2a*-HET, and DM. Scale indicates log2
795 fold change of depleted (blue) to enriched (yellow) H3K4me3. We analyzed amygdala
796 tissue from 2 to 3 animals for each genotype (see Methods).
797
798 **Figure 3. Similar transcriptomes between the *Kdm5c*-KO and *Kmt2a*-HET and**
799 **rescue effect in DM. (A)** Transcriptome comparison across three mutant genotypes
800 relative to WT, represented as log2 mean normalized counts from DESeq2 (91).
801 Differentially-expressed (DE) genes were determined using a threshold of *p*-value <
802 0.01 as previously described (31). **(B)** Log2 fold change relative to WT, of expression of

803 all 466 DE genes identified (136 *Kmt2a*-HET + 127 *Kdm5c*-KO + 203 DM). Scale
804 indicates log2 fold change of down- (blue) to up- (yellow) regulated expression.
805 Histogram on scale indicates count of genes in each color category. **(C)** Overlap
806 between DE genes across genotypes. **(D)** Intersection of DE genes from reciprocal
807 categories in single mutants. **(C)** Volcano plots depicting rescue effect in DM on *Kdm5c*-
808 KO and *Kmt2a*-HET DE genes. DM gene expression plotted in grey, as log2 fold
809 change and *p*-value in DM compared to WT. Genes identified as DE in either single
810 mutant shown as open circles. Any of these genes that fell within the $p > 0.1$ cutoff (red
811 shaded box) were considered rescued in DM. Dashed line depicts $p = 0.01$ threshold for
812 determining DE genes. **(F)** Log2 fold change relative to WT, of expression of all 118
813 rescued genes. Scale indicates log2 fold change of down- (blue) to up- (yellow)
814 regulated expression. Histogram on scale indicates count of genes in each color
815 category. We analyzed amygdala tissue from 3 animals for each genotype (see
816 Methods).
817
818 **Figure 4. Altered dendrite morphology of *Kdm5c*-KO and *Kmt2a*-HET was**
819 **reversed in DM animals. (A)** Representative images of basolateral amygdala (BLA)
820 pyramidal neurons across all genotypes, depicting overall neuron morphology including
821 dendrite lengths and dendritic spines. Scale bars represent: 100μm (above, whole
822 neuron image), 10μm (below, spine image). **(B and C)** Left panel: Total dendrite lengths
823 **(B)** or spine density **(C)** (mean ± 95% *$p<0.05$, ****$p<0.0001$, One-way ANOVA). Right
824 panel: Difference between group means (mean ± 95% confidence intervals, *$p<0.05$,
825 **$p<0.01$, ***$p<0.001$, ****$p<0.0001$ in Tukey multiple comparison test). **(D)**

826 Quantification of spine morphology subtypes, represented as percent of total spines
827 counted. At least 20 neurons from 4 animals per genotype were quantified.
828
829 **Figure 5. Deficit of memory-related behavior in *Kdm5c*-KO and its rescue in DM.**
830 **(A)** Contextual fear conditioning test. Left panel: Freezing levels after shock on test day
831 (mean ± SEM, *$p < 0.05$ in One-way ANOVA). Right panel: Difference between group
832 means of freezing (mean ± 95% confidence intervals, *$p<0.05$ in Least Significant
833 Difference (LSD) test). **(B)** Novel object recognition test. Left panel: Preference for novel
834 versus familiar object (mean ± SEM, *$p < 0.05$ in One-way ANOVA). Right panel:
835 Difference between group means of freeze response (mean ± 95% confidence intervals,
836 *$p<0.05$ in Least Significant Difference (LSD) test). **(C)** Response to mild foot-shock
837 (mean ± 95% confidence intervals, no statistical significance [n.s.], One-way ANOVA).
838 **(D)** Locomotor activity (mean ± 95% confidence intervals, no statistical significance
839 [n.s.], One-way ANOVA). N=21 WT, N=16 *Kmt2a*-HET, N=16 *Kdm5c*-KO, and N=12
840 DM animals were used for all studies.
841

842 **Figure 6. Differential impacts of double mutation in social behavior. (A)** Three
843 chamber test for social interaction. Left panel: preference for stranger versus toy mouse
844 (mean ± SEM, **$p < 0.01$ in One-way ANOVA). Right panel: Difference between group
845 means of preference (mean ± 95% confidence intervals, *$p<0.05$, **$p<0.01$ in Least
846 Significant Difference (LSD) test). **(B)** Tube test for social dominance. Proportion of wins
847 in matches of each mutant versus WT. Numbers on colored bars represent total number
848 of wins for WT (grey, above) or each mutant (below) in every matchup. **$p<0.01$,

849 ***p<0.001, Exact binomial test. **(C-L)** Resident intruder test. **(C)** Left panel: average
850 number of all aggressive behaviors (mean ± SEM, *p < 0.05 in One-way ANOVA). Right
851 panel: Difference between group means of aggressive behaviors (mean ± 95%
852 confidence intervals, *p<0.05 in Least Significant Difference (LSD) test). **(D-H)** Individual
853 aggressive behaviors (mean ± SEM, **p < 0.01 in One-way ANOVA). N.s. depicts no
854 statistical difference. **(I)** Left panel: average number of all submissive behaviors (mean ±
855 SEM, *p < 0.05 in One-way ANOVA). Right panel: Difference between group means of
856 submissive behaviors (mean ± 95% confidence intervals, **p<0.01, ***p<0.001 in Least
857 Significant Difference (LSD) test). **(J-L)** Individual submissive behaviors (mean ± SEM,
858 **p < 0.01 in One-way ANOVA). N.s. depicts no statistical difference. N=21 WT, N=16
859 *Kmt2a*-HET, N=16 *Kdm5c*-KO, and N=12 DM animals were used for all studies.
860
861 **Supplementary Figure 1. Expression of KMT2A and KDM5C. (A)** Expression of
862 *Kmt2a* and *Kdm5c*, from FACS-sorted single cells of mouse visual cortex, shown in
863 reads per kilobase of transcript per million mapped reads (RPKM). Neuronal cells:
864 GABAergic (GABA), Glutamatergic (Glu). Non-neuronal cells: astrocytes (A); endothelial
865 cells (E); microglia (M), oligodendrocyte precursor cells (OPC); oligodendrocytes (O);
866 smooth muscle cells (SMC). Image credit: Broad Institute "Single Cell Portal"
867 transcriptome of adult mouse visual cortex (38). **(B)** Expression of *Kmt2a* and *Kdm5c*
868 mRNA from adult mouse brain, shown in log2 of raw expression value from *in situ*
869 hybridization. Brain regions: Isocortex, olfactory areas (OLF), hippocampal formation
870 (HPF), cortical subplate (CTXsp), striatum (STR), pallidum (PAL), thalamus (TH),
871 hypothalamus (HY), midbrain (MB), pons (P), medulla (MY), cerebellum (CB). Image

872 credit: Allen Institute, Allen Mouse Brain Atlas (2004) (34). **(C)** Expression of *KMT2A*
873 and *KDM5C* transcripts, from developing and adult human brains, shown in RPKM.
874 Human development and adulthood were split into the following Periods: 1-7 fetal
875 development; 8-9 birth and infancy; 10-11 childhood; 12 adolescence; and 13-15
876 adulthood. Image credit: Human Brain Transcriptome Atlas (36, 105)
877
878 **Supplementary Figure 2. Genotype confirmation and gross brain morphology of**
879 **mutant mice. (A-B)** RNA-seq read coverage of *Kmt2a* **(A)** and *Kdm5c* **(B)** genes, and
880 targeted exons (highlight). **(C)** Genotyping using genomic DNA, confirming presence of
881 *Kmt2a* and/or *Kdm5c* deleted alleles ("del") only in appropriate genotypes. **(D)** Western
882 blot for KDM5C protein. Stars indicate non-specific bands present in all samples.
883 GAPDH shown for equal loading. **(E)** Serial brain sections 30 μm thick stained with
884 DAPI to mark nuclei. Sections shown at Bregma regions 1.41, 0.49, -2.15, and -2.91
885 mm (top to bottom). Regions highlighted: anterior forceps of the corpus callosum (fmi),
886 caudate putamen (CPu), corpus callosum (cc), lateral ventricle (LV), piriform cortex
887 (Pir), olfactory tubercle (Tu), hippocampal fields CA1 and CA2, dentate gyrus (DG),
888 anteromedial nucleus (AM), third ventricle (3V), substantia nigra pars reticularis (SNR).
889 Scale bar: 1mm.
890
891 **Supplementary Figure 3. H3K4me3 in the amygdala. (A)** Western blot of whole brain
892 lysates showing unchanged global H3K4 methylation across genotypes. Total histone
893 H3 was detected using an antibody recognizing the C-terminus of H3, and used as a
894 control for equal loading. **(B)** Validation of H3K4me3 ChIP-seq specificity. Barcode

895 reads originating from spike-in nucleosomes were counted. The two synthetic
896 nucleosomes with the H3K4me3 barcodes dominated all ChIP samples, with
897 H3K4me1/2 nucleosomes rarely detected. **(C)** H3K4me3 coverage in *Kmt2a*-HET,
898 *Kdm5c*-KO, or DM compared to WT at promoters (± 1 kb of transcription start sites). **(D)**
899 Distribution of all H3K4me3 peaks across the genome, in all genotypes. **(E-F)** Log2 fold
900 change of H3K4me3 coverage across genotypes relative to WT, at *Kmt2a*-HET DMRs
901 **(E)** or *Kdm5c*-KO DMRs **(F)**. Scale indicates log2 fold change of depleted (blue) to
902 enriched (yellow) H3K4me3. **(G-H)** H3K4me3 coverage of individual replicates at
903 *Kmt2a*-HET DMRs **(G)** or *Kdm5c*-KO DMRs **(H)** in all genotypes. Scale indicates low
904 (light) to high (dark) H3K4me3 coverage. **(I-J)** Top five mammalian transcription factor
905 motifs identified in *Kmt2a*-HET **(I)** and *Kdm5c*-KO **(J)** DMRs.
906
907 **Supplementary Figure 4. Additional analyses of the RNA-seq dataset. (A)** ERCC
908 spike-in dose-response curves in each genotype, plotting expected vs. observed
909 transcript counts. Each dot represents a spike-in RNA molecule. **(B)** Comparison of
910 mean normalized counts of *Kdm5c*-KO from present study (grey dots) with our previous
911 RNA-seq approach (31). Previously identified up- (yellow) and down- (blue) regulated
912 genes show consistent patterns in the present study. **(C)** Intersection of up- and down-
913 regulated DE genes across genotypes. **(D)** Fold change of DE genes across genotypes.
914 Boxplot features depict: box, interquartile range (IQR); line, median; whiskers,
915 proportion of IQR past low and high quartiles. **(E-F)** Volcano plots depicting similarity of
916 gene expression patterns in *Kdm5c*-KO and *Kmt2a*-HET DE genes. Genes identified as
917 DE in either single mutant shown as open circles. By and large, genes identified as up

918 (yellow) or down (blue) in one category are expressed in the same direction in the
919 reciprocal genotype. Dashed line depicts p = 0.01 threshold for determining DE genes.
920
921 **Supplementary Figure 5. Expression of genes that are activity-dependent, cell-**
922 **type specific, or developmentally regulated, in mutant amygdala. (A-B)** Expression
923 of activity-dependent genes, which we previously identified by nascent RNA sequencing
924 using cortical neurons in response to bicuculine (3,785 genes) **(A)**, or TTX (2,416
925 genes) **(B)** (106). Spearman Rank-order correlation test for all comparisons showed no
926 linear relationship between fold changes of either set of activity-dependent genes and
927 DE genes in the mutant transcriptomes, indicating normal expression of activity-
928 dependent genes in all three genotypes. **(C)** DE gene expression across cell types.
929 Genes enriched in seven cell types: astrocytes (A), neurons (N), microglia/macrophages
930 (M), oligodendrocyte precursor cells (Op), newly formed oligodendrocytes (On),
931 myelinating oligodendrocytes (Om), endothelial cells (E). Data were obtained from
932 Zhang et al. (93). None of the DE genes in the mutant amygdala show strong bias to a
933 particular cell type. Boxplot features depict: box, interquartile range (IQR); line, median;
934 whiskers, proportion of IQR past low and high quartiles. **(D-E)** We examined human
935 adult male amygdala gene expression over time, from embryonic to adult ages.
936 Preconception weeks (PCW), months (mo), years (yr). We examined trajectory of
937 neurogeneisis (GO:0050769) or synaptic (GO:0007268) genes throughout normal
938 development **(D)**. As expected, synaptic genes showed upward shift, while
939 neurogenesis genes exhibited downward shift in their expression during the
940 development. When we plotted the expression of our DE genes across genotypes

941 throughout normal development, we did not find noticeable trends, except that DM
942 down-regulated genes were more highly expressed compared to DE genes in other
943 genotypes **(E)**. Data credit: Allen Institute, BrainSpan Atlas of the Developing Human
944 Brain (2010) (94).
945
946 **Supplementary Figure 6. Integrative analysis of ChIP-seq and RNA-seq (A)**
947 Expression of genes associated with promoter- or intragenic-DMRs. **(B)** RNA-seq read
948 depth and H3K4me3 ChIP-seq read depth at 5c-KO intergenic DMRs, across
949 genotypes. **(C)** H3K4me3 coverage at promoter regions of differentially expressed (DE)
950 genes. **(D)** H3K4me3 coverage at promoter regions of rescued genes. Boxplot features
951 depict: box, interquartile range (IQR); line, median; notch, confidence interval for
952 median; whiskers, proportion of IQR past low and high quartiles.
953
954 **Supplementary Figure 7. Schematic of dendrite spine subtype analysis. (A)**
955 Projection image of a dendritic segment from a series of Z stack images derived from
956 BLA pyramidal cells. Numerical marks adjacent to corresponding spine subtypes,
957 represented as: 1. Filopodia, 2. Thin, 3, Stubby, 4. Mushroom, and 5. Branched
958
959 **Supplementary Figure 8. Behaviors during resident-intruder test.** Differences
960 between group means all aggressive **(A-E)** and submissive **(F-H)** behaviors (mean ±
961 95% confidence intervals, *p<0.05, **p<0.01 in Least Significant Difference (LSD) test).
962

963 **Supplementary Figure 9. Molecular alterations unique to DM mice. (A)**
964 Representative genome browser view of extended H3K4me3 boundary observed at
965 some DM DMRs. **(B)** Volcano plots depicting larger gene misregulation effects in the
966 DM transcriptome. Transcriptome of *Kmt2a*-HET or *Kdm5c*-KO plotted as grey dots.
967 Genes identified as DE in DM shown as colored open circles. A majority of these genes
968 fell below the line of significance in either single mutant, indicating DM leads to the
969 misregulation of genes that were previously not DE in either *Kmt2a*-HET or *Kdm5c*-KO.
970 Dashed line depicts $p = 0.01$ threshold for determining DE genes. **(C)** Fold change of
971 DM DE genes across genotypes. DM up- and down-regulated genes were expressed in
972 the same direction in each single mutant, though DM leads to a more pronounced up- or
973 down-regulation effect. Boxplot features depict: box, interquartile range (IQR); line,
974 median; whiskers, proportion of IQR past low and high quartiles.
975
976 **Supplementary Table 1. Gene annotation enrichment analysis of rescued genes.**
977 Functional annotation clustering of gene ontology biological process groups (GO:BP),
978 for 118 rescued genes in DM. Analysis performed by the database for annotation,
979 visualization and integrated discovery (DAVID).

980 **References**

981 1. Faundes V, Newman WG, Bernardini L, Canham N, Clayton-Smith J, Dallapiccola B, et
982 al. Histone Lysine Methylases and Demethylases in the Landscape of Human
983 Developmental Disorders. *Am J Hum Genet.* 2018;102(1):175-87.
984 2. De Rubeis S, He X, Goldberg AP, Poultney CS, Samocha K, Ercument Cicek A, et al.
985 Synaptic, transcriptional and chromatin genes disrupted in autism. *Nature.*
986 2014;515(7526):209-15.
987 3. Iossifov I, O'Roak BJ, Sanders SJ, Ronemus M, Krumm N, Levy D, et al. The
988 contribution of de novo coding mutations to autism spectrum disorder. *Nature.*
989 2014;515(7526):216-21.
990 4. Kouzarides T. Chromatin modifications and their function. *Cell.* 2007;128(4):693-
991 705.
992 5. Taverna SD, Li H, Ruthenburg AJ, Allis CD, and Patel DJ. How chromatin-binding
993 modules interpret histone modifications: lessons from professional pocket pickers.
994 *Nat Struct Mol Biol.* 2007;14(11):1025-40.
995 6. Allis CD, Berger SL, Cote J, Dent S, Jenuwien T, Kouzarides T, et al. New
996 nomenclature for chromatin-modifying enzymes. *Cell.* 2007;131(4):633-6.
997 7. Iwase S, Berube NG, Zhou Z, Kasri NN, Battaglioli E, Scandaglia M, et al. Epigenetic
998 Etiology of Intellectual Disability. *The Journal of neuroscience : the official journal of*
999 *the Society for Neuroscience.* 2017;37(45):10773-82.
1000 8. Ronan JL, Wu W, and Crabtree GR. From neural development to cognition:
1001 unexpected roles for chromatin. *Nat Rev Genet.* 2013;14(5):347-59.
1002 9. Iwase S, and Shi Y. Histone and DNA modifications in mental retardation. *Progress in*
1003 *drug research Fortschritte der Arzneimittelforschung Progres des recherches*
1004 *pharmaceutiques.* 2011;67:147-73.
1005 10. Barski A, Cuddapah S, Cui K, Roh TY, Schones DE, Wang Z, et al. High-resolution
1006 profiling of histone methylations in the human genome. *Cell.* 2007;129(4):823-37.
1007 11. Heintzman ND, Stuart RK, Hon G, Fu Y, Ching CW, Hawkins RD, et al. Distinct and
1008 predictive chromatin signatures of transcriptional promoters and enhancers in the
1009 human genome. *Nat Genet.* 2007;39(3):311-8.
1010 12. Vermeulen M, Mulder KW, Denissov S, Pijnappel WW, van Schaik FM, Varier RA, et
1011 al. Selective anchoring of TFIID to nucleosomes by trimethylation of histone H3
1012 lysine 4. *Cell.* 2007;131(1):58-69.
1013 13. Lauberth SM, Nakayama T, Wu X, Ferris AL, Tang Z, Hughes SH, et al. H3K4me3
1014 Interactions with TAF3 Regulate Preinitiation Complex Assembly and Selective Gene
1015 Activation. *Cell.* 2013;152(5):1021-36.
1016 14. Local A, Huang H, Albuquerque CP, Singh N, Lee AY, Wang W, et al. Identification of
1017 H3K4me1-associated proteins at mammalian enhancers. *Nat Genet.* 2018;50(1):73-
1018 82.
1019 15. Cheung I, Shulha HP, Jiang Y, Matevossian A, Wang J, Weng Z, et al. Developmental
1020 regulation and individual differences of neuronal H3K4me3 epigenomes in the
1021 prefrontal cortex. *Proceedings of the National Academy of Sciences of the United*
1022 *States of America.* 2010;107(19):8824-9.

1023 16. Shulha HP, Cheung I, Whittle C, Wang J, Virgil D, Lin CL, et al. Epigenetic signatures
1024 of autism: trimethylated H3K4 landscapes in prefrontal neurons. *Arch Gen*
1025 *Psychiatry.* 2012;69(3):314-24.
1026 17. Shulha HP, Crisci JL, Reshetov D, Tushir JS, Cheung I, Bharadwaj R, et al. Human-
1027 specific histone methylation signatures at transcription start sites in prefrontal
1028 neurons. *PLoS biology.* 2012;10(11):e1001427.
1029 18. Vallianatos CN, and Iwase S. Disrupted intricacy of histone H3K4 methylation in
1030 neurodevelopmental disorders. *Epigenomics.* 2015;7(3):503-19.
1031 19. Alarcon JM, Malleret G, Touzani K, Vronskaya S, Ishii S, Kandel ER, et al. Chromatin
1032 acetylation, memory, and LTP are impaired in CBP+/- mice: a model for the
1033 cognitive deficit in Rubinstein-Taybi syndrome and its amelioration. *Neuron.*
1034 2004;42(6):947-59.
1035 20. Bjornsson HT, Benjamin JS, Zhang L, Weissman J, Gerber EE, Chen YC, et al. Histone
1036 deacetylase inhibition rescues structural and functional brain deficits in a mouse
1037 model of Kabuki syndrome. *Science translational medicine.* 2014;6(256):256ra135.
1038 21. Park J, Thomas S, and Munster PN. Epigenetic modulation with histone deacetylase
1039 inhibitors in combination with immunotherapy. *Epigenomics.* 2015;7(4):641-52.
1040 22. Strom SP, Lozano R, Lee H, Dorrani N, Mann J, O'Lague PF, et al. De Novo variants in
1041 the KMT2A (MLL) gene causing atypical Wiedemann-Steiner syndrome in two
1042 unrelated individuals identified by clinical exome sequencing. *BMC Med Genet.*
1043 2014;15:49.
1044 23. Jones WD, Dafou D, McEntagart M, Woollard WJ, Elmslie FV, Holder-Espinasse M, et
1045 al. De Novo Mutations in MLL Cause Wiedemann-Steiner Syndrome. *American*
1046 *Journal of Human Genetics.* 2012;91(2):358-64.
1047 24. Claes S, Devriendt K, Van Goethem G, Roelen L, Meireleire J, Raeymaekers P, et al.
1048 Novel syndromic form of X-linked complicated spastic paraplegia. *Am J Med Genet.*
1049 2000;94(1):1-4.
1050 25. Jensen LR, Amende M, Gurok U, Moser B, Gimmel V, Tzschach A, et al. Mutations in
1051 the JARID1C gene, which is involved in transcriptional regulation and chromatin
1052 remodeling, cause X-linked mental retardation. *Am J Hum Genet.* 2005;76(2):227-36.
1053 26. Adegbola A, Gao H, Sommer S, and Browning M. A novel mutation in JARID1C/SMCX
1054 in a patient with autism spectrum disorder (ASD). *American journal of medical*
1055 *genetics Part A.* 2008;146A(4):505-11.
1056 27. Vallianatos CN, Farrehi C, Friez MJ, Burmeister M, Keegan CE, and Iwase S. Altered
1057 Gene-Regulatory Function of KDM5C by a Novel Mutation Associated With Autism
1058 and Intellectual Disability. *Front Mol Neurosci.* 2018;11:104.
1059 28. Gupta S, Kim SY, Artis S, Molfese DL, Schumacher A, Sweatt JD, et al. Histone
1060 methylation regulates memory formation. *The Journal of neuroscience : the official*
1061 *journal of the Society for Neuroscience.* 2010;30(10):3589-99.
1062 29. Jakovcevski M, Ruan H, Shen EY, Dincer A, Javidfar B, Ma Q, et al. Neuronal
1063 Kmt2a/Mll1 histone methyltransferase is essential for prefrontal synaptic plasticity
1064 and working memory. *The Journal of neuroscience : the official journal of the Society*
1065 *for Neuroscience.* 2015;35(13):5097-108.
1066 30. Kerimoglu C, Sakib MS, Jain G, Benito E, Burkhardt S, Capece V, et al. KMT2A and
1067 KMT2B Mediate Memory Function by Affecting Distinct Genomic Regions. *Cell Rep.*
1068 2017;20(3):538-48.

1069 31. Iwase S, Brookes E, Agarwal S, Badeaux AI, Ito H, Vallianatos CN, et al. A Mouse
1070 Model of X-linked Intellectual Disability Associated with Impaired Removal of
1071 Histone Methylation. *Cell reports.* 2016.
1072 32. Scandaglia M, Lopez-Atalaya JP, Medrano-Fernandez A, Lopez-Cascales MT, Del
1073 Blanco B, Lipinski M, et al. Loss of Kdm5c Causes Spurious Transcription and
1074 Prevents the Fine-Tuning of Activity-Regulated Enhancers in Neurons. *Cell reports.*
1075 2017;21(1):47-59.
1076 33. Hawrylycz MJ, Lein ES, Guillozet-Bongaarts AL, Shen EH, Ng L, Miller JA, et al. An
1077 anatomically comprehensive atlas of the adult human brain transcriptome. *Nature.*
1078 2012;489(7416):391-9.
1079 34. Lein ES, Hawrylycz MJ, Ao N, Ayres M, Bensinger A, Bernard A, et al. Genome-wide
1080 atlas of gene expression in the adult mouse brain. *Nature.* 2007;445(7124):168-76.
1081 35. Zhang XQ, Wang ZL, Poon MW, and Yang JH. Spatial-temporal transcriptional
1082 dynamics of long non-coding RNAs in human brain. *Hum Mol Genet.*
1083 2017;26(16):3202-11.
1084 36. Pletikos M, Sousa AM, Sedmak G, Meyer KA, Zhu Y, Cheng F, et al. Temporal
1085 specification and bilaterality of human neocortical topographic gene expression.
1086 *Neuron.* 2014;81(2):321-32.
1087 37. Johnson MB, Kawasawa YI, Mason CE, Krsnik Z, Coppola G, Bogdanovic D, et al.
1088 Functional and evolutionary insights into human brain development through global
1089 transcriptome analysis. *Neuron.* 2009;62(4):494-509.
1090 38. Tasic B, Menon V, Nguyen TN, Kim TK, Jarsky T, Yao Z, et al. Adult mouse cortical cell
1091 taxonomy revealed by single cell transcriptomics. *Nature neuroscience.*
1092 2016;19(2):335-46.
1093 39. Cao F, Townsend EC, Karatas H, Xu J, Li L, Lee S, et al. Targeting MLL1 H3K4
1094 methyltransferase activity in mixed-lineage leukemia. *Mol Cell.* 2014;53(2):247-61.
1095 40. Dou YL, Milne TA, Ruthenburg AJ, Lee S, Lee JW, Verdine GL, et al. Regulation of
1096 MLL1 H3K4 methyltransferase activity by its core components. *Nature Structural &*
1097 *Molecular Biology.* 2006;13(8):713-9.
1098 41. Iwase S, Lan F, Bayliss P, de la Torre-Ubieta L, Huarte M, Qi HH, et al. The X-linked
1099 mental retardation gene SMCX/JARID1C defines a family of histone H3 lysine 4
1100 demethylases. *Cell.* 2007;128(6):1077-88.
1101 42. Tahiliani M, Mei PC, Fang R, Leonor T, Rutenberg M, Shimizu F, et al. The histone
1102 H3K4 demethylase SMCX links REST target genes to X-linked mental retardation.
1103 *Nature.* 2007;447(7144):601-+.
1104 43. Shah RN, Grzybowski AT, Cornett EM, Johnstone AL, Dickson BM, Boone BA, et al.
1105 Examining the Roles of H3K4 Methylation States with Systematically Characterized
1106 Antibodies. *Molecular cell.* 2018;72(1):162-77 e7.
1107 44. Jaworski E, and Routh A. ClickSeq: Replacing Fragmentation and Enzymatic Ligation
1108 with Click-Chemistry to Prevent Sequence Chimeras. *Methods Mol Biol.*
1109 2018;1712:71-85.
1110 45. Zhang H, Gayen S, Xiong J, Zhou B, Shanmugam AK, Sun Y, et al. MLL1 Inhibition
1111 Reprograms Epiblast Stem Cells to Naive Pluripotency. *Cell stem cell.*
1112 2016;18(4):481-94.
1113 46. Outchkourov NS, Muino JM, Kaufmann K, van Ijcken WF, Groot Koerkamp MJ, van
1114 Leenen D, et al. Balancing of histone H3K4 methylation states by the Kdm5c/SMCX

1115 histone demethylase modulates promoter and enhancer function. *Cell reports.*
1116 2013;3(4):1071-9.
1117 47. S G, E M, Y M-N, CN V, RS P, PM G, et al. biorxiv: Cold Spring Harbor Laboratory;
1118 2017.
1119 48. Nakamura K, Kodera H, Akita T, Shiina M, Kato M, Hoshino H, et al. De Novo
1120 mutations in GNAO1, encoding a Gαo subunit of heterotrimeric G proteins, cause
1121 epileptic encephalopathy. *Am J Hum Genet.* 2013;93(3):496-505.
1122 49. Kulkarni N, Tang S, Bhardwaj R, Bernes S, and Grebe TA. Progressive Movement
1123 Disorder in Brothers Carrying a GNAO1 Mutation Responsive to Deep Brain
1124 Stimulation. *J Child Neurol.* 2016;31(2):211-4.
1125 50. Lessel D, Gehbauer C, Bramswig NC, Schluth-Bolard C, Venkataramanappa S, van
1126 Gassen KLI, et al. BCL11B mutations in patients affected by a neurodevelopmental
1127 disorder with reduced type 2 innate lymphoid cells. *Brain.* 2018;141(8):2299-311.
1128 51. Webb EA, AlMutair A, Kelberman D, Bacchelli C, Chanudet E, Lescai F, et al. ARNT2
1129 mutation causes hypopituitarism, post-natal microcephaly, visual and renal
1130 anomalies. *Brain.* 2013;136(Pt 10):3096-105.
1131 52. Slavotinek AM, Stone EM, Mykytyn K, Heckenlively JR, Green JS, Heon E, et al.
1132 Mutations in MKKS cause Bardet-Biedl syndrome. *Nat Genet.* 2000;26(1):15-6.
1133 53. Katsanis N, Beales PL, Woods MO, Lewis RA, Green JS, Parfrey PS, et al. Mutations in
1134 MKKS cause obesity, retinal dystrophy and renal malformations associated with
1135 Bardet-Biedl syndrome. *Nat Genet.* 2000;26(1):67-70.
1136 54. Schaefer E, Durand M, Stoetzel C, Doray B, Viville B, Hellé S, et al. Molecular
1137 diagnosis reveals genetic heterogeneity for the overlapping MKKS and BBS
1138 phenotypes. *Eur J Med Genet.* 2011;54(2):157-60.
1139 55. Stone DL, Slavotinek A, Bouffard GG, Banerjee-Basu S, Baxevanis AD, Barr M, et al.
1140 Mutation of a gene encoding a putative chaperonin causes McKusick-Kaufman
1141 syndrome. *Nat Genet.* 2000;25(1):79-82.
1142 56. Tsurusaki Y, Okamoto N, Ohashi H, Kosho T, Imai Y, Hibi-Ko Y, et al. Mutations
1143 affecting components of the SWI/SNF complex cause Coffin-Siris syndrome. *Nat*
1144 *Genet.* 2012;44(4):376-8.
1145 57. Guissart C, Latypova X, Rollier P, Khan TN, Stamberger H, McWalter K, et al. Dual
1146 Molecular Effects of Dominant RORA Mutations Cause Two Variants of Syndromic
1147 Intellectual Disability with Either Autism or Cerebellar Ataxia. *Am J Hum Genet.*
1148 2018;102(5):744-59.
1149 58. Miyazaki T, Hashimoto K, Uda A, Sakagami H, Nakamura Y, Saito SY, et al.
1150 Disturbance of cerebellar synaptic maturation in mutant mice lacking BSRPs, a novel
1151 brain-specific receptor-like protein family. *FEBS Lett.* 2006;580(17):4057-64.
1152 59. Penzes P, Cahill ME, Jones KA, VanLeeuwen JE, and Woolfrey KM. Dendritic spine
1153 pathology in neuropsychiatric disorders. *Nat Neurosci.* 2011;14(3):285-93.
1154 60. Dierssen M, and Ramakers GJ. Dendritic pathology in mental retardation: from
1155 molecular genetics to neurobiology. *Genes Brain Behav.* 2006;5 Suppl 2:48-60.
1156 61. Xu X, Miller EC, and Pozzo-Miller L. Dendritic spine dysgenesis in Rett syndrome.
1157 *Front Neuroanat.* 2014;8:97.
1158 62. Irwin SA, Galvez R, and Greenough WT. Dendritic spine structural anomalies in
1159 fragile-X mental retardation syndrome. *Cereb Cortex.* 2000;10(10):1038-44.

1160 63. Arikkath J. Molecular mechanisms of dendrite morphogenesis. *Front Cell Neurosci.*
1161 2012;6:61.
1162 64. Maren S. Neurobiology of Pavlovian fear conditioning. *Annual review of neuroscience.*
1163 2001;24:897-931.
1164 65. Wang F, Kessels HW, and Hu H. The mouse that roared: neural mechanisms of social
1165 hierarchy. *Trends Neurosci.* 2014;37(11):674-82.
1166 66. Kim B, Colon E, Chawla S, Vandenberg LN, and Suvorov A. Endocrine disruptors alter
1167 social behaviors and indirectly influence social hierarchies via changes in body
1168 weight. *Environ Health.* 2015;14:64.
1169 67. Varholick JA, Bailoo JD, Palme R, and Würbel H. Phenotypic variability between
1170 Social Dominance Ranks in laboratory mice. *Sci Rep.* 2018;8(1):6593.
1171 68. Eissenberg JC, and Shilatifard A. Histone H3 lysine 4 (H3K4) methylation in
1172 development and differentiation. *Dev Biol.* 2010;339(2):240-9.
1173 69. Shilatifard A. The COMPASS family of histone H3K4 methylases: mechanisms of
1174 regulation in development and disease pathogenesis. *Annual review of biochemistry.*
1175 2012;81:65-95.
1176 70. Mishra S, Van Rechem C, Pal S, Clarke TL, Chakraborty D, Mahan SD, et al. Cross-talk
1177 between Lysine-Modifying Enzymes Controls Site-Specific DNA Amplifications. *Cell.*
1178 2018;175(6):1716.
1179 71. Cao K, Collings CK, Morgan MA, Marshall SA, Rendleman EJ, Ozark PA, et al. An
1180 Mll4/COMPASS-Lsd1 epigenetic axis governs enhancer function and pluripotency
1181 transition in embryonic stem cells. *Sci Adv.* 2018;4(1):eaap8747.
1182 72. Wiedemann HR. Genital overgrowth in the EMG syndrome. *Am J Med Genet.*
1183 1989;32(2):255-6.
1184 73. Felix-Ortiz AC, and Tye KM. Amygdala inputs to the ventral hippocampus
1185 bidirectionally modulate social behavior. *J Neurosci.* 2014;34(2):586-95.
1186 74. McCann KE, Sinkiewicz DM, Rosenhauer AM, Beach LQ, and Huhman KL.
1187 Transcriptomic Analysis Reveals Sex-Dependent Expression Patterns in the
1188 Basolateral Amygdala of Dominant and Subordinate Animals After Acute Social
1189 Conflict. *Mol Neurobiol.* 2018.
1190 75. Levinson DM, Reeves DL, and Buchanan DR. Reductions in aggression and
1191 dominance status in guinea pigs following bilateral lesions in the basolateral
1192 amygdala or lateral septum. *Physiol Behav.* 1980;25(6):963-71.
1193 76. McGregor A, and Herbert J. Differential effects of excitotoxic basolateral and
1194 corticomedial lesions of the amygdala on the behavioural and endocrine responses
1195 to either sexual or aggression-promoting stimuli in the male rat. *Brain Res.*
1196 1992;574(1-2):9-20.
1197 77. Felix-Ortiz AC, Burgos-Robles A, Bhagat ND, Leppla CA, and Tye KM. Bidirectional
1198 modulation of anxiety-related and social behaviors by amygdala projections to the
1199 medial prefrontal cortex. *Neuroscience.* 2016;321:197-209.
1200 78. McMahon KA, Hiew SY, Hadjur S, Veiga-Fernandes H, Menzel U, Price AJ, et al. Mll
1201 has a critical role in fetal and adult hematopoietic stem cell self-renewal. *Cell stem*
1202 *cell.* 2007;1(3):338-45.
1203 79. Brind'Amour J, Liu S, Hudson M, Chen C, Karimi MM, and Lorincz MC. An ultra-low-
1204 input native ChIP-seq protocol for genome-wide profiling of rare cell populations.
1205 *Nat Commun.* 2015;6:6033.

1206 80. Grzybowski AT, Chen Z, and Ruthenburg AJ. Calibrating ChIP-Seq with Nucleosomal
1207 Internal Standards to Measure Histone Modification Density Genome Wide. *Mol Cell.*
1208 2015;58(5):886-99.
1209 81. Zhang Y, Liu T, Meyer CA, Eeckhoute J, Johnson DS, Bernstein BE, et al. Model-based
1210 analysis of ChIP-Seq (MACS). *Genome biology.* 2008;9(9):R137.
1211 82. Heinz S, Benner C, Spann N, Bertolino E, Lin YC, Laslo P, et al. Simple combinations
1212 of lineage-determining transcription factors prime cis-regulatory elements required
1213 for macrophage and B cell identities. *Molecular cell.* 2010;38(4):576-89.
1214 83. Mudunuri U, Che A, Yi M, and Stephens RM. bioDBnet: the biological database
1215 network. *Bioinformatics.* 2009;25(4):555-6.
1216 84. Edgar R, Domrachev M, and Lash AE. Gene Expression Omnibus: NCBI gene
1217 expression and hybridization array data repository. *Nucleic Acids Res.*
1218 2002;30(1):207-10.
1219 85. Dobin A, Davis CA, Schlesinger F, Drenkow J, Zaleski C, Jha S, et al. STAR: ultrafast
1220 universal RNA-seq aligner. *Bioinformatics.* 2013;29(1):15-21.
1221 86. Smith T, Heger A, and Sudbery I. UMI-tools: modeling sequencing errors in Unique
1222 Molecular Identifiers to improve quantification accuracy. *Genome Res.*
1223 2017;27(3):491-9.
1224 87. Liao Y, Smyth GK, and Shi W. featureCounts: an efficient general purpose program
1225 for assigning sequence reads to genomic features. *Bioinformatics.* 2014;30(7):923-
1226 30.
1227 88. Ramírez F, Dündar F, Diehl S, Grüning BA, and Manke T. deepTools: a flexible
1228 platform for exploring deep-sequencing data. *Nucleic Acids Res.* 2014;42(Web Server
1229 issue):W187-91.
1230 89. Ramírez F, Ryan DP, Grüning B, Bhardwaj V, Kilpert F, Richter AS, et al. deepTools2:
1231 a next generation web server for deep-sequencing data analysis. *Nucleic Acids Res.*
1232 2016;44(W1):W160-5.
1233 90. Anders S, and Huber W. Differential expression analysis for sequence count data.
1234 *Genome biology.* 2010;11(10):R106.
1235 91. Love MI, Huber W, and Anders S. Moderated estimation of fold change and
1236 dispersion for RNA-seq data with DESeq2. *Genome Biol.* 2014;15(12):550.
1237 92. Khomtchouk BB, Hennessy JR, and Wahlestedt C. shinyheatmap: Ultra fast low
1238 memory heatmap web interface for big data genomics. *PLoS One.*
1239 2017;12(5):e0176334.
1240 93. Zhang Y, Chen K, Sloan SA, Bennett ML, Scholze AR, O'Keeffe S, et al. An RNA-
1241 Sequencing Transcriptome and Splicing Database of Glia, Neurons, and Vascular
1242 Cells of the Cerebral Cortex. *J Neurosci.* 2014;34(36):11929-47.
1243 94. Miller JA, Ding SL, Sunkin SM, Smith KA, Ng L, Szafer A, et al. Transcriptional
1244 landscape of the prenatal human brain. *Nature.* 2014;508(7495):199-206.
1245 95. Shmelkov SV, Hormigo A, Jing D, Proenca CC, Bath KG, Milde T, et al. Slitrk5
1246 deficiency impairs corticostriatal circuitry and leads to obsessive-compulsive-like
1247 behaviors in mice. *Nature medicine.* 2010;16(5):598-602, 1p following
1248 96. Vogel-Ciernia A, and Wood MA. Examining object location and object recognition
1249 memory in mice. *Curr Protoc Neurosci.* 2014;69:8.31.1-17.
1250 97. Tchessalova D, and Tronson NC. Memory deficits in males and females long after
1251 subchronic immune challenge. *Neurobiol Learn Mem.* 2019.

98. Keiser AA, Turnbull LM, Darian MA, Feldman DE, Song I, and Tronson NC. Sex Differences in Context Fear Generalization and Recruitment of Hippocampus and Amygdala during Retrieval. *Neuropsychopharmacology.* 2017;42(2):397-407.
99. Crawley JN. Mouse behavioral assays relevant to the symptoms of autism. *Brain Pathol.* 2007;17(4):448-59.
100. Zhou T, Zhu H, Fan Z, Wang F, Chen Y, Liang H, et al. History of winning remodels thalamo-PFC circuit to reinforce social dominance. *Science.* 2017;357(6347):162-8.
101. Larrieu T, Cherix A, Duque A, Rodrigues J, Lei H, Gruetter R, et al. Hierarchical Status Predicts Behavioral Vulnerability and Nucleus Accumbens Metabolic Profile Following Chronic Social Defeat Stress. *Curr Biol.* 2017;27(14):2202-10.e4.
102. Moretti P, Bouwknecht JA, Teague R, Paylor R, and Zoghbi HY. Abnormalities of social interactions and home-cage behavior in a mouse model of Rett syndrome. *Hum Mol Genet.* 2005;14(2):205-20.
103. Guzmán YF, Tronson NC, Jovasevic V, Sato K, Guedea AL, Mizukami H, et al. Fear-enhancing effects of septal oxytocin receptors. *Nat Neurosci.* 2013;16(9):1185-7.
104. Miczek KA, Maxson SC, Fish EW, and Faccidomo S. Aggressive behavioral phenotypes in mice. *Behav Brain Res.* 2001;125(1-2):167-81.
105. Kang HJ, Kawasawa YI, Cheng F, Zhu Y, Xu X, Li M, et al. Spatio-temporal transcriptome of the human brain. *Nature.* 2011;478(7370):483-9.
106. Garay P, Chen A, Tsukahara T, Kohen R, Althaus C, Wallner M, et al.: Biorxiv; 2019.

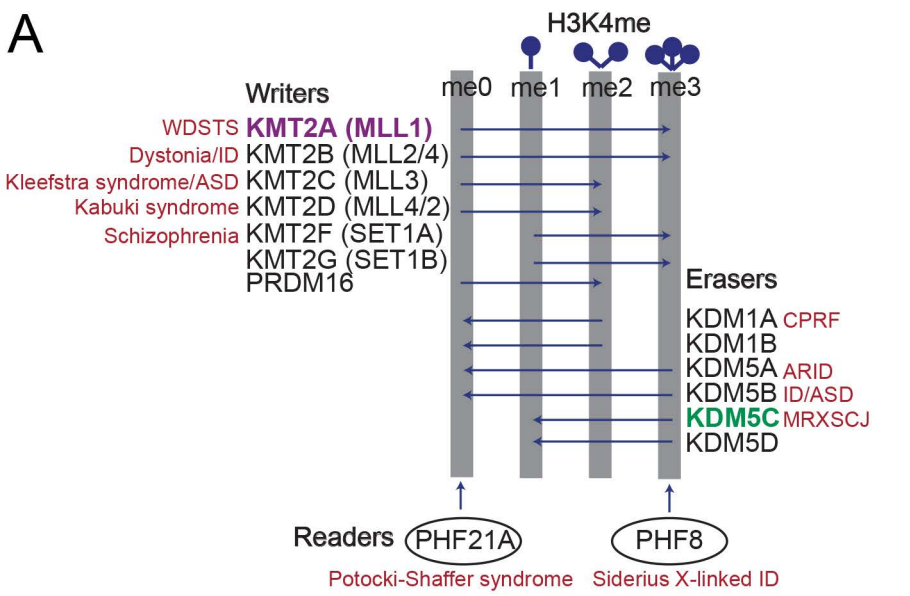

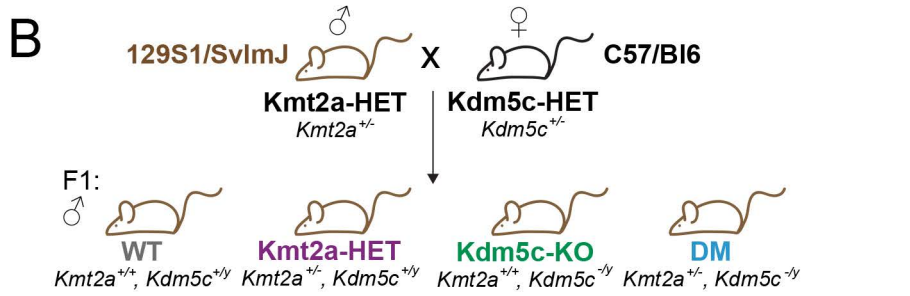

C

Number of offspring across 30 litters (% total males)			
WT	2a-HET	5c-KO	DM
17	16	21	14
(25%)	(23%)	(31%)	(21%)

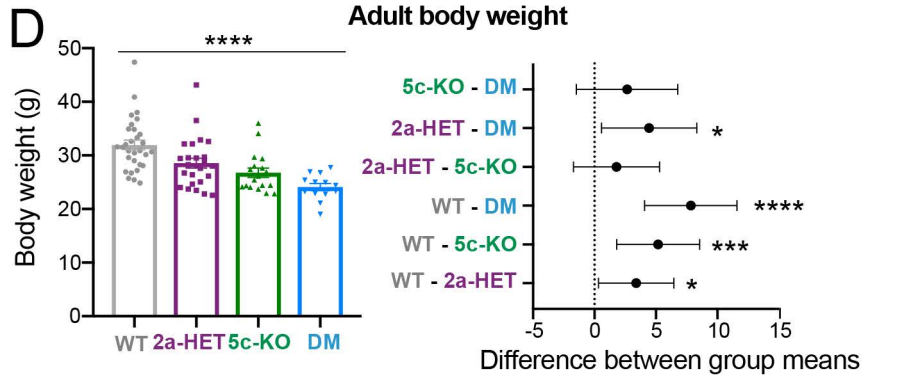

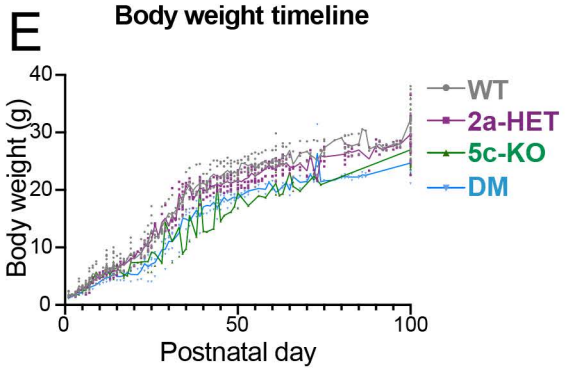

Figure 1

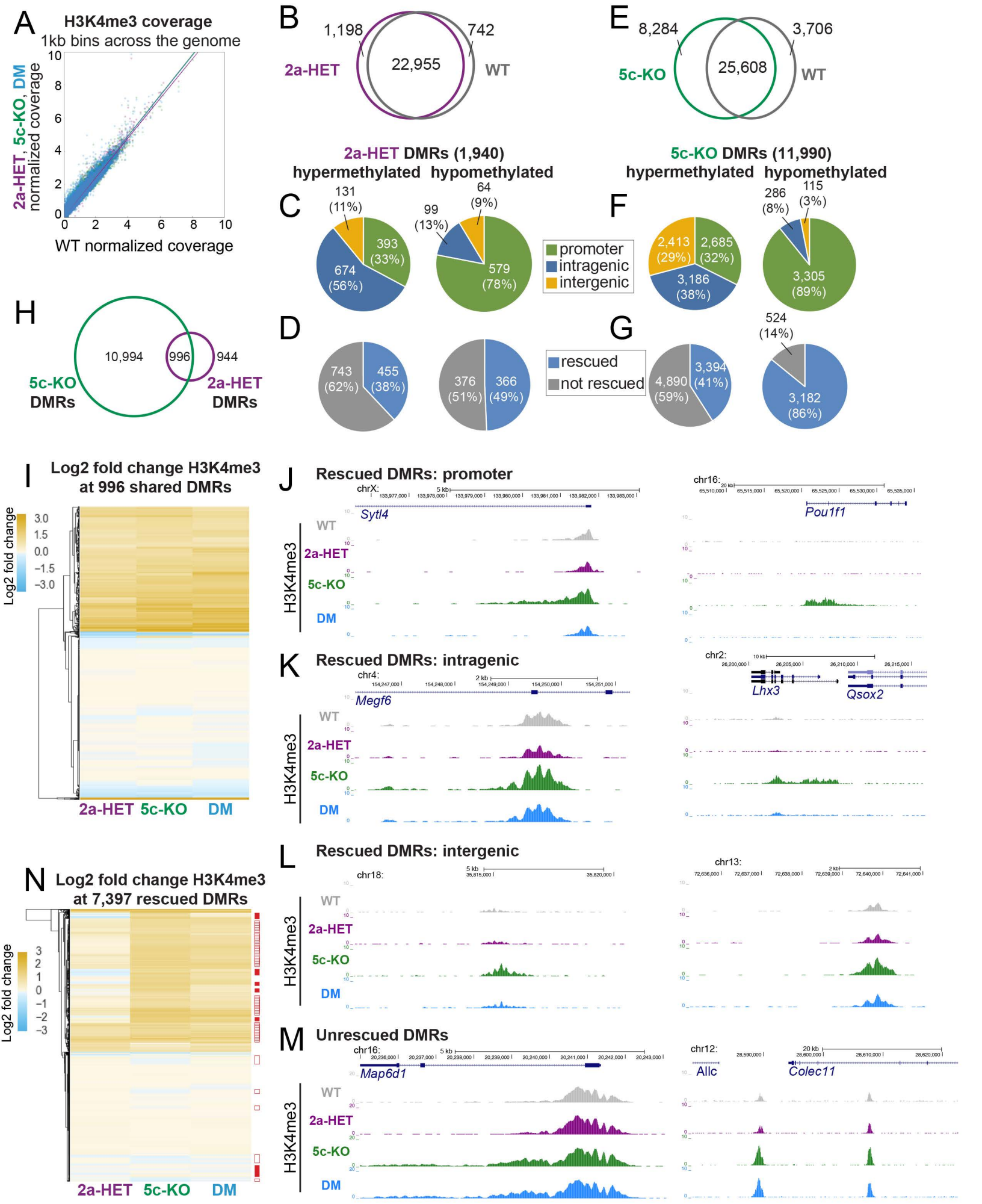
A
H3K4me3 coverage
1kb bins across the genome
2a-HET, 5c-KO, DM normalized coverage
WT normalized coverage
B
1,198
22,955
742
2a-HET
WT
E
8,284
25,608
3,706
5c-KO
WT
2a-HET DMRs (1,940)
hypermethylated
hypomethylated
5c-KO DMRs (11,990)
hypermethylated
hypomethylated
C
131 (11%)
393 (33%)
674 (56%)
99 (13%)
64 (9%)
579 (78%)
promoter
intragenic
intergenic
F
2,413 (29%)
2,685 (32%)
3,186 (38%)
286 (8%)
115 (3%)
3,305 (89%)
D
743 (62%)
455 (38%)
376 (51%)
366 (49%)
rescued
not rescued
G
4,890 (59%)
3,394 (41%)
524 (14%)
3,182 (86%)
H
10,994
996
944
5c-KO DMRs
2a-HET DMRs
I
Log2 fold change H3K4me3 at 996 shared DMRs
Log2 fold change
3.0
1.5
0.0
−1.5
−3.0
2a-HET
5c-KO
DM
J
Rescued DMRs: promoter
chrX:
Sytl4
chr16:
Pou1f1
H3K4me3
WT
2a-HET
5c-KO
DM
K
Rescued DMRs: intragenic
chr4:
Megf6
chr2:
Lhx3
Qsox2
L
Rescued DMRs: intergenic
chr18:
chr13:
N
Log2 fold change H3K4me3 at 7,397 rescued DMRs
Log2 fold change
3
2
1
0
−1
−2
−3
M
Unrescued DMRs
chr16:
Map6d1
chr12:
Allc
Colec11

Figure 2

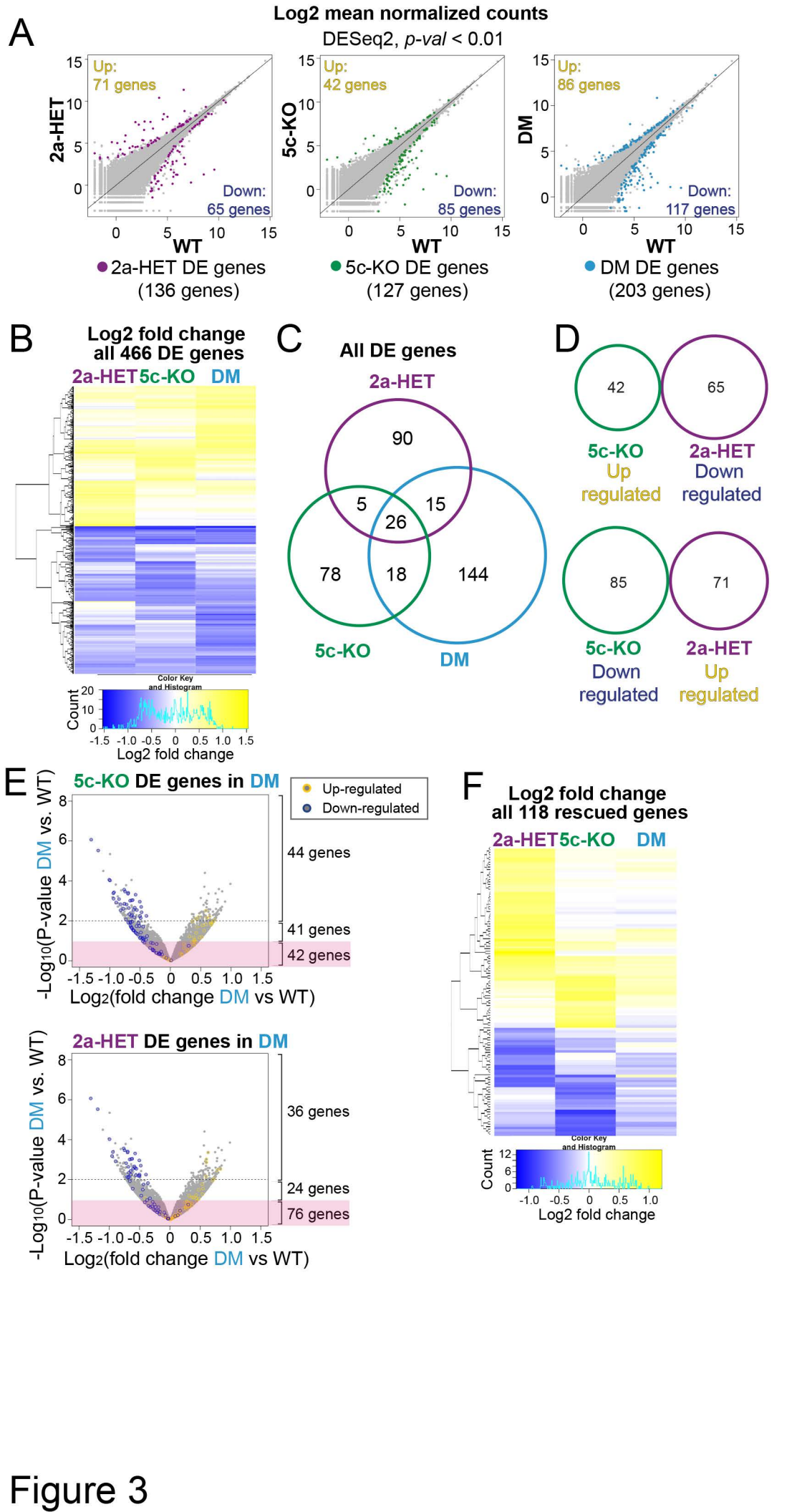
A
Log2 mean normalized counts
DESeq2, p-val < 0.01
Up: 71 genes
Down: 65 genes
2a-HET
WT
Up: 42 genes
Down: 85 genes
5c-KO
WT
Up: 86 genes
Down: 117 genes
DM
WT
2a-HET DE genes (136 genes)
5c-KO DE genes (127 genes)
DM DE genes (203 genes)
B
Log2 fold change all 466 DE genes
2a-HET 5c-KO DM
Color Key and Histogram
Count
Log2 fold change
C
All DE genes
2a-HET
90
5
15
26
78
18
144
5c-KO
DM
D
42
65
5c-KO Up regulated
2a-HET Down regulated
85
71
5c-KO Down regulated
2a-HET Up regulated
E
5c-KO DE genes in DM
Up-regulated
Down-regulated
44 genes
41 genes
42 genes
-Log10(P-value DM vs. WT)
Log2(fold change DM vs WT)
2a-HET DE genes in DM
36 genes
24 genes
76 genes
-Log10(P-value DM vs. WT)
Log2(fold change DM vs WT)
F
Log2 fold change all 118 rescued genes
2a-HET 5c-KO DM
Color Key and Histogram
Count
Log2 fold change

Figure 3

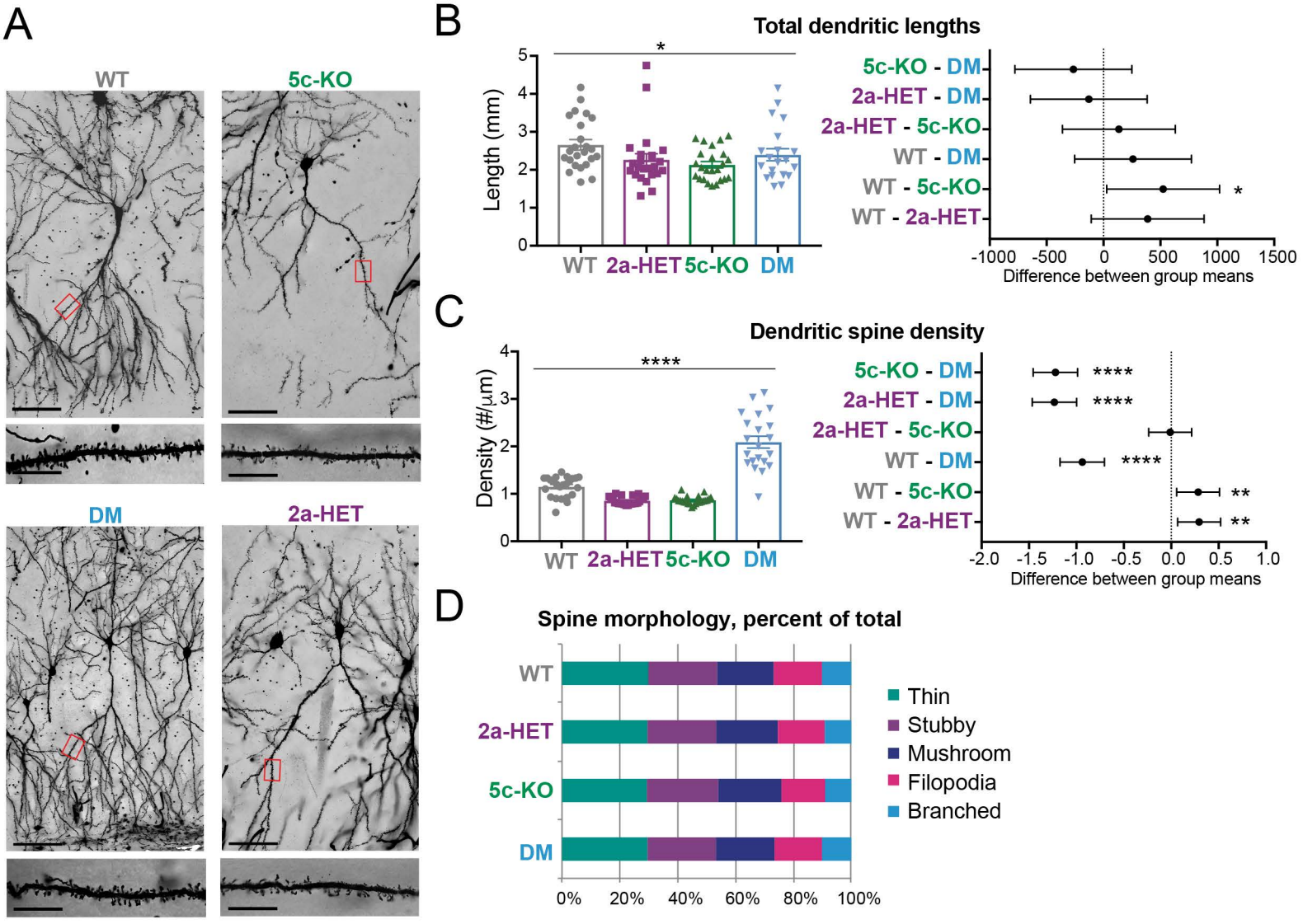
A
WT
5c-KO
DM
2a-HET
B
Total dendritic lengths
Length (mm)
*
WT 2a-HET 5c-KO DM
5c-KO - DM
2a-HET - DM
2a-HET - 5c-KO
WT - DM
WT - 5c-KO
WT - 2a-HET
-1000 -500 0 500 1000 1500
Difference between group means
C
Dendritic spine density
Density (#/µm)
****
WT 2a-HET 5c-KO DM
5c-KO - DM
2a-HET - DM
2a-HET - 5c-KO
WT - DM
WT - 5c-KO
WT - 2a-HET
-2.0 -1.5 -1.0 -0.5 0.0 0.5 1.0
Difference between group means
D
Spine morphology, percent of total
WT
2a-HET
5c-KO
DM
0% 20% 40% 60% 80% 100%
Thin
Stubby
Mushroom
Filopodia
Branched

Figure 4

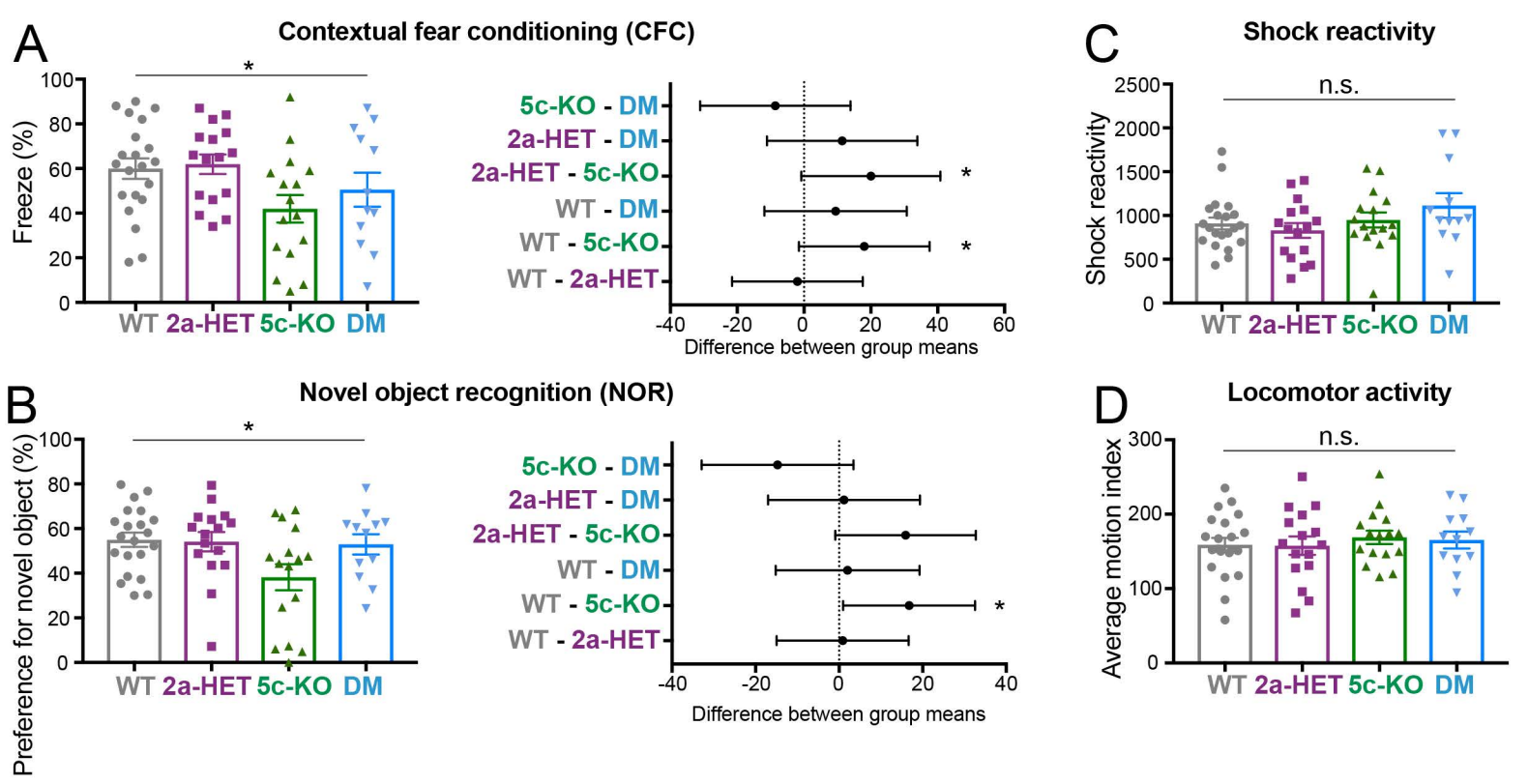
A
Contextual fear conditioning (CFC)
Freeze (%)
100
80
60
40
20
0
*
WT
2a-HET
5c-KO
DM
5c-KO - DM
2a-HET - DM
2a-HET - 5c-KO
WT - DM
WT - 5c-KO
WT - 2a-HET
*
*
-40
-20
0
20
40
60
Difference between group means
C
Shock reactivity
Shock reactivity
2500
2000
1500
1000
500
0
n.s.
WT
2a-HET
5c-KO
DM
B
Novel object recognition (NOR)
Preference for novel object (%)
100
80
60
40
20
0
*
WT
2a-HET
5c-KO
DM
5c-KO - DM
2a-HET - DM
2a-HET - 5c-KO
WT - DM
WT - 5c-KO
WT - 2a-HET
*
-40
-20
0
20
40
Difference between group means
D
Locomotor activity
Average motion index
300
200
100
0
n.s.
WT
2a-HET
5c-KO
DM

Figure 5

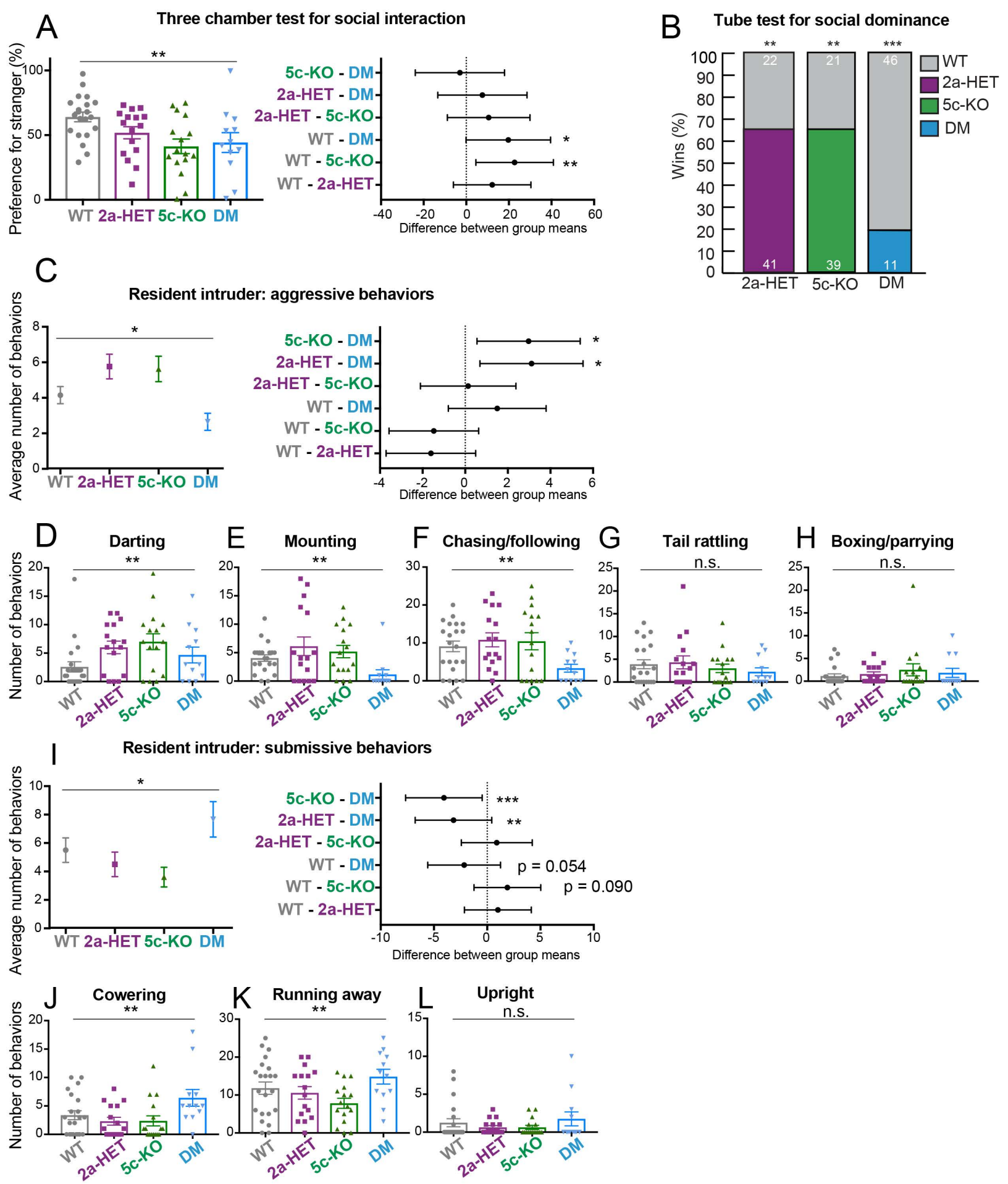
A
Three chamber test for social interaction
Preference for stranger (%)
WT 2a-HET 5c-KO DM
5c-KO - DM
2a-HET - DM
2a-HET - 5c-KO
WT - DM
WT - 5c-KO
WT - 2a-HET
Difference between group means
B
Tube test for social dominance
Wins (%)
2a-HET 5c-KO DM
WT
2a-HET
5c-KO
DM
C
Resident intruder: aggressive behaviors
Average number of behaviors
D
Darting
E
Mounting
F
Chasing/following
G
Tail rattling
H
Boxing/parrying
n.s.
Number of behaviors
I
Resident intruder: submissive behaviors
p = 0.054
p = 0.090
J
Cowering
K
Running away
L
Upright

Figure 6

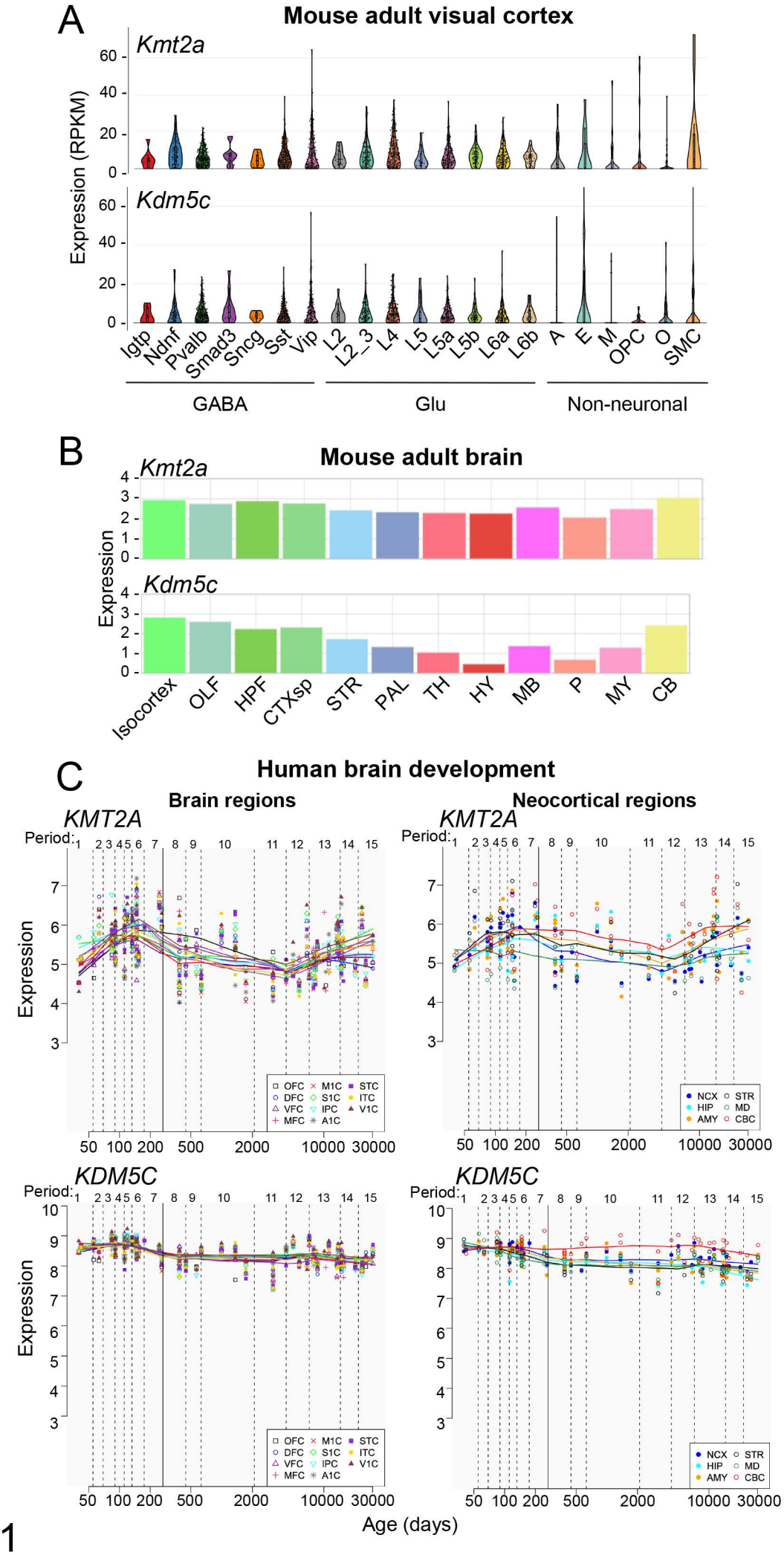

Supplementary Figure 1

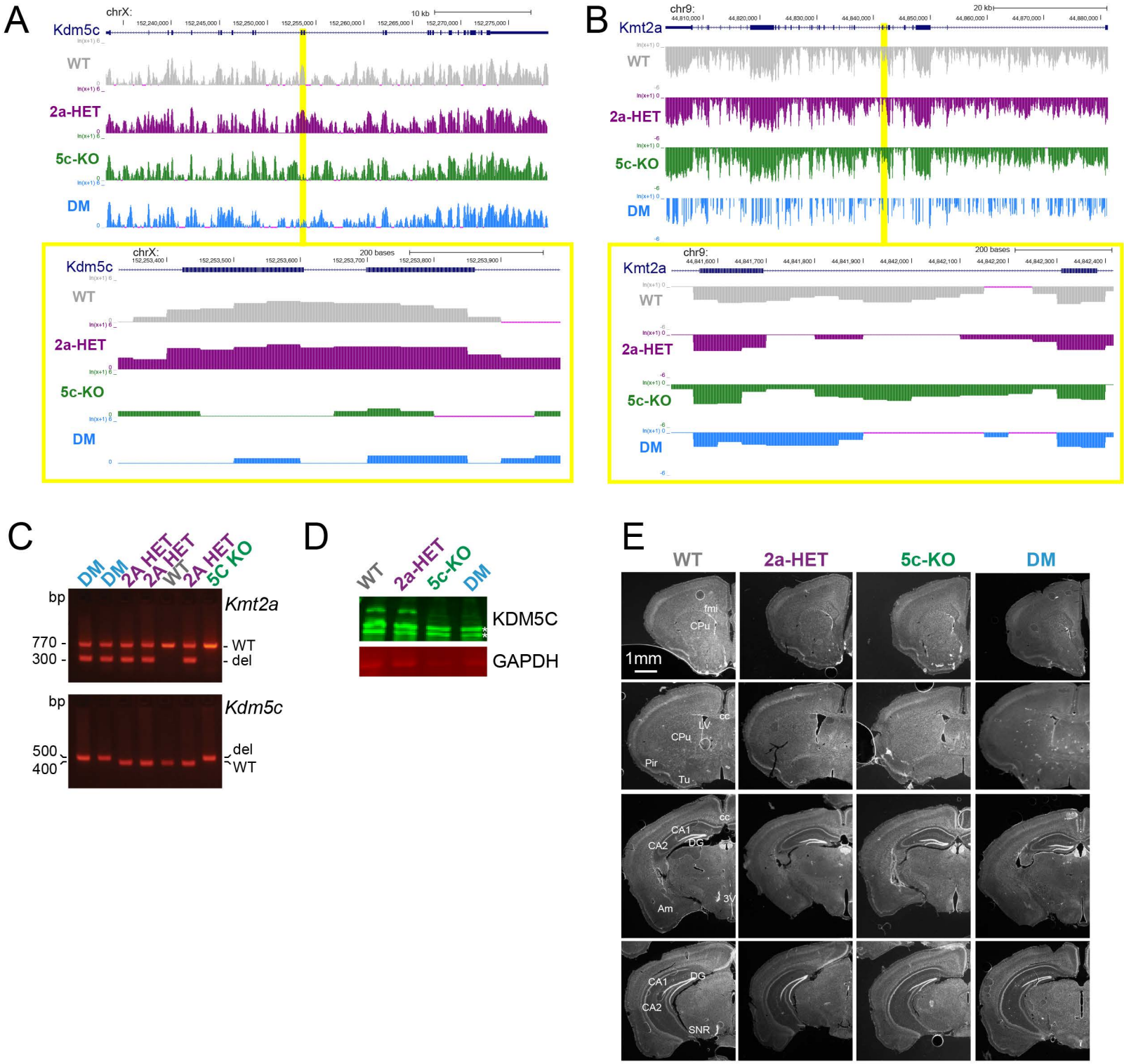

Supplementary Figure 2

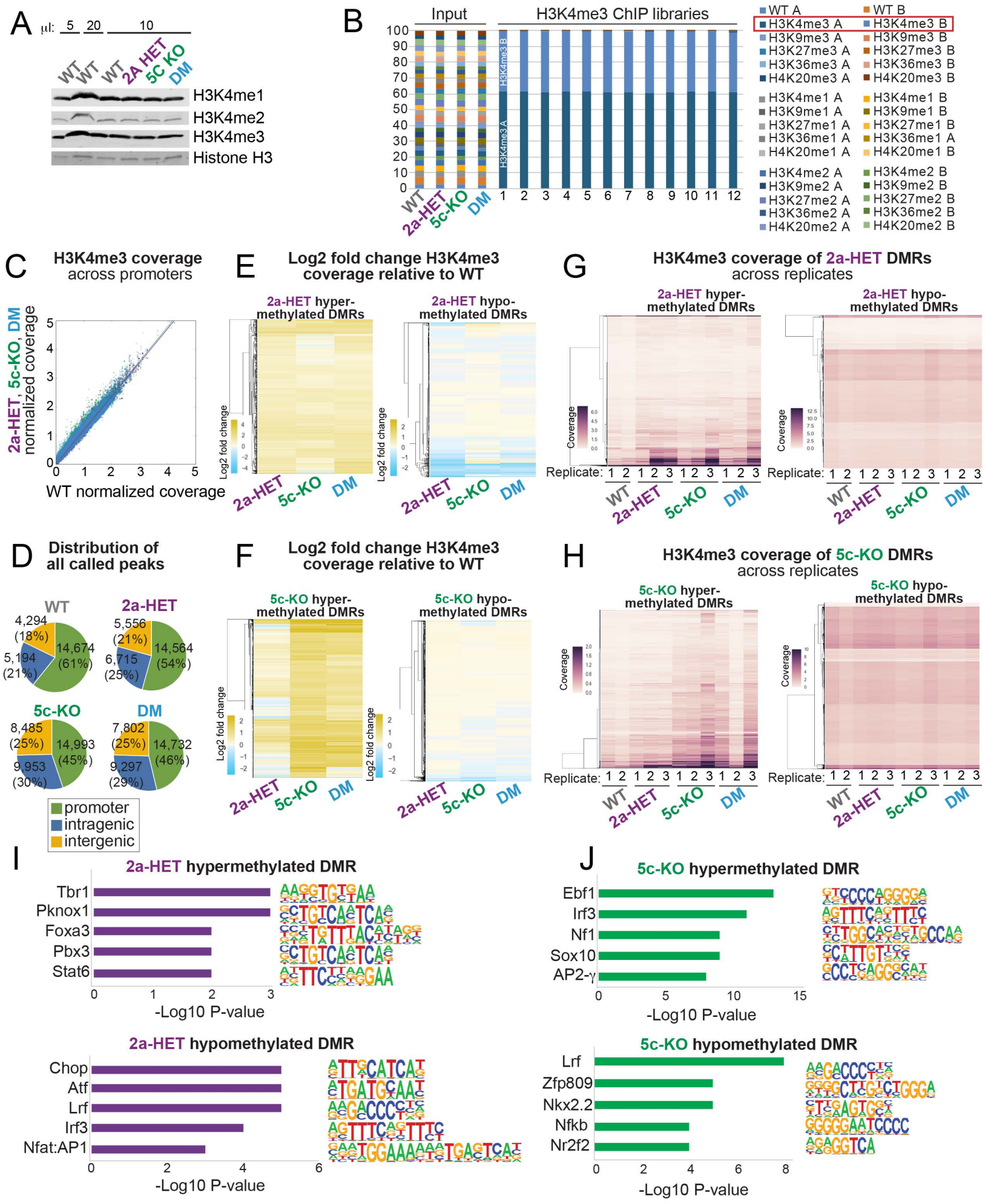

Supplementary Figure 3

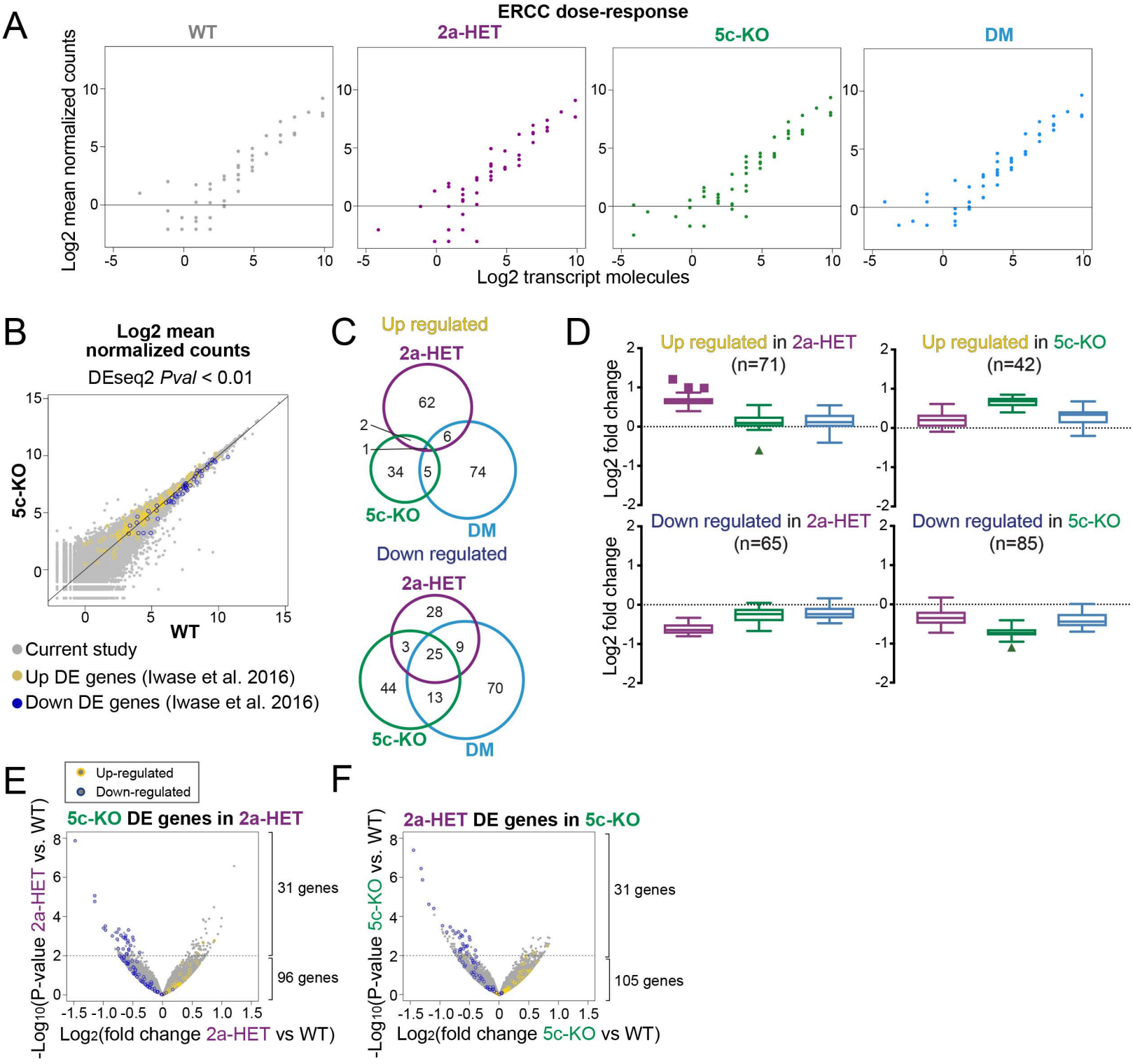

Supplementary Figure 4

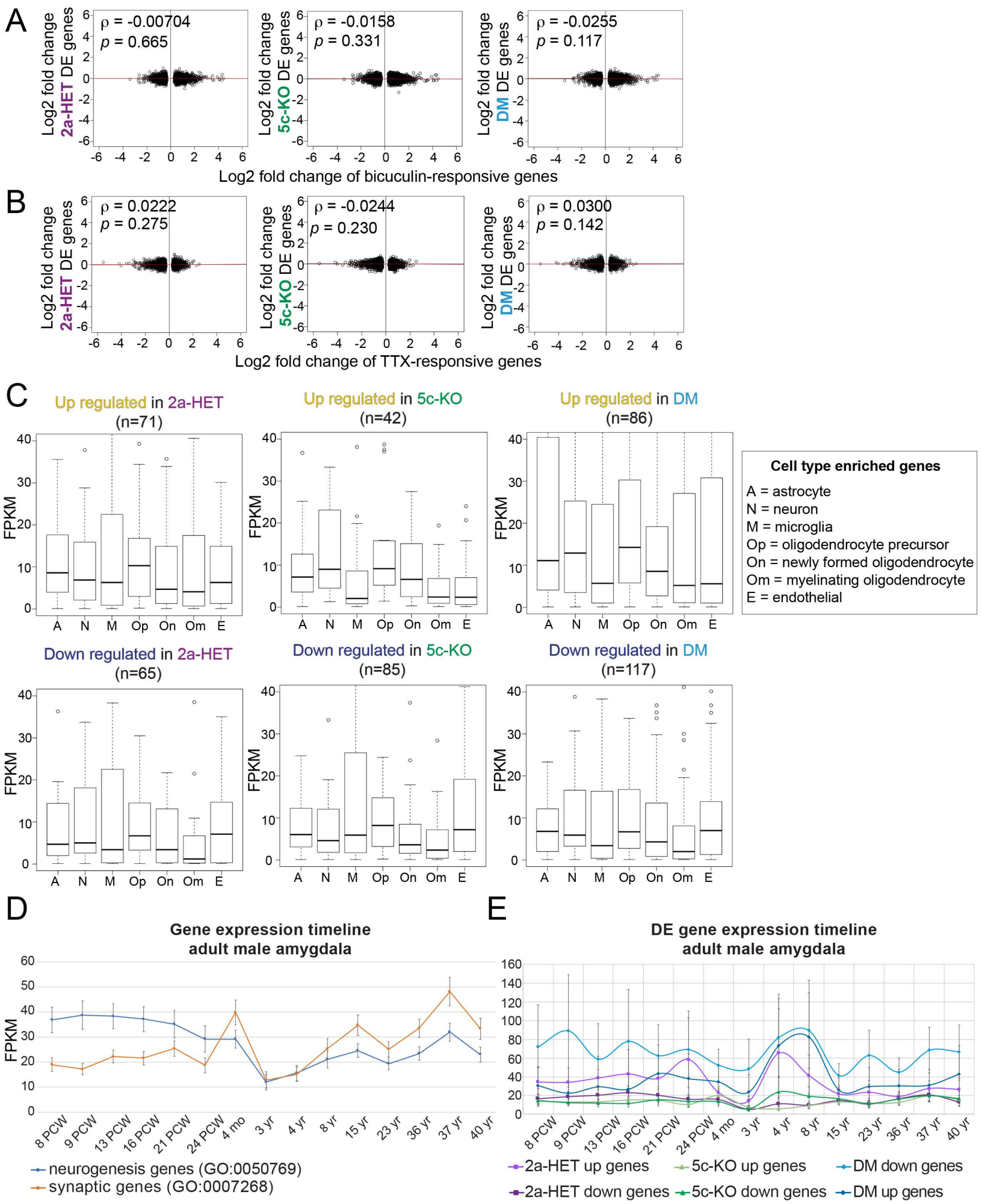

Supplementary Figure 5

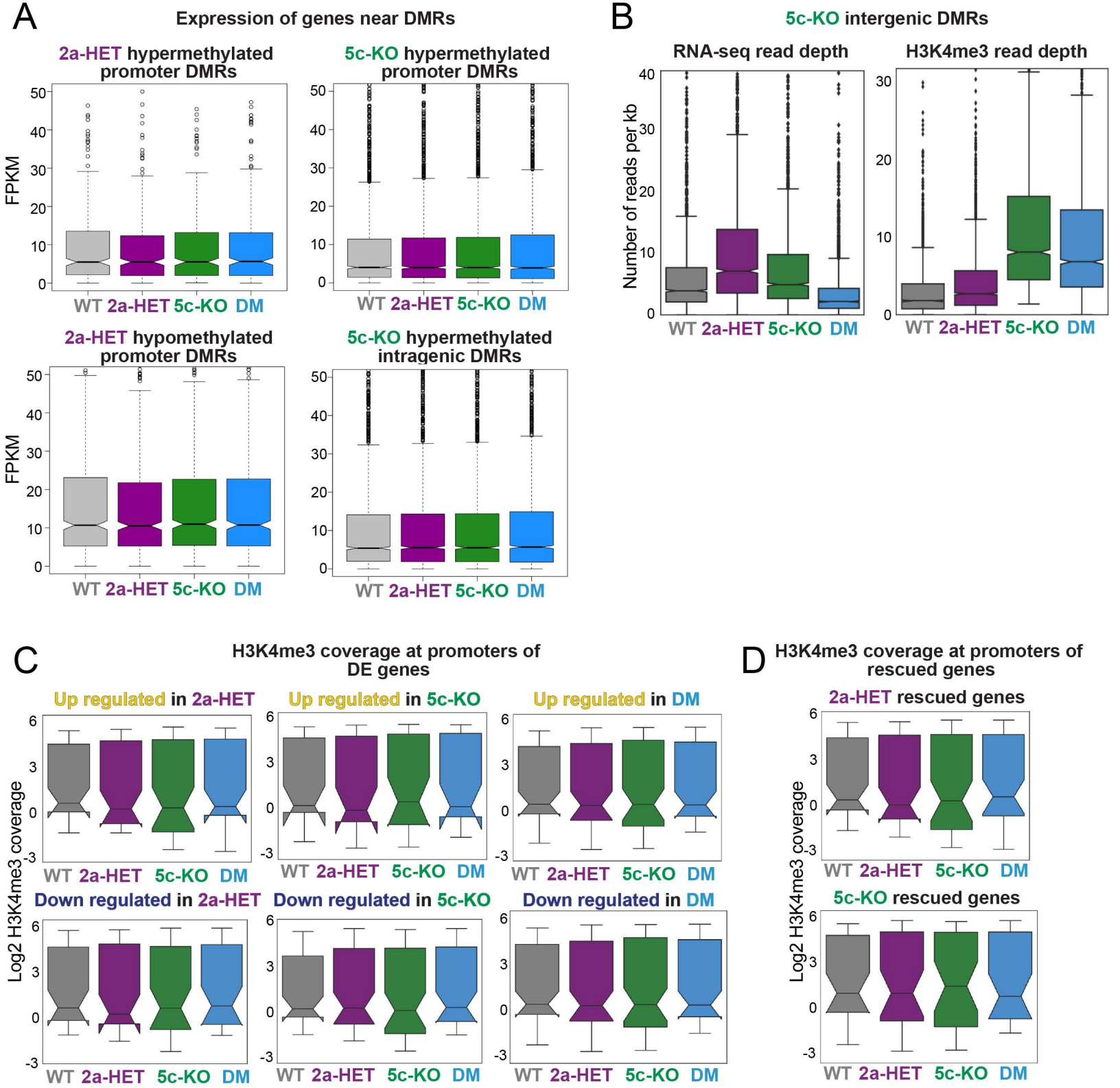

Supplementary Figure 6

A

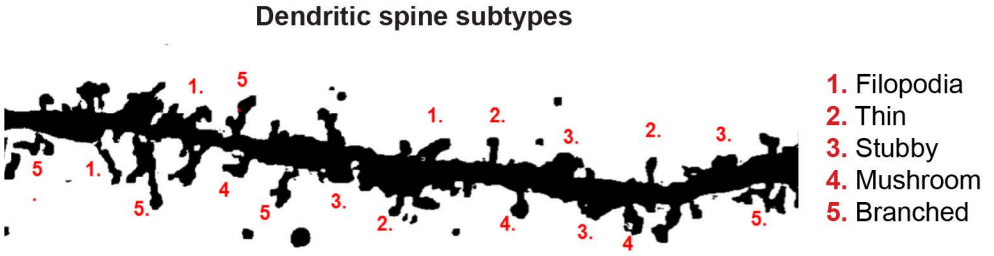

Supplementary Figure 7

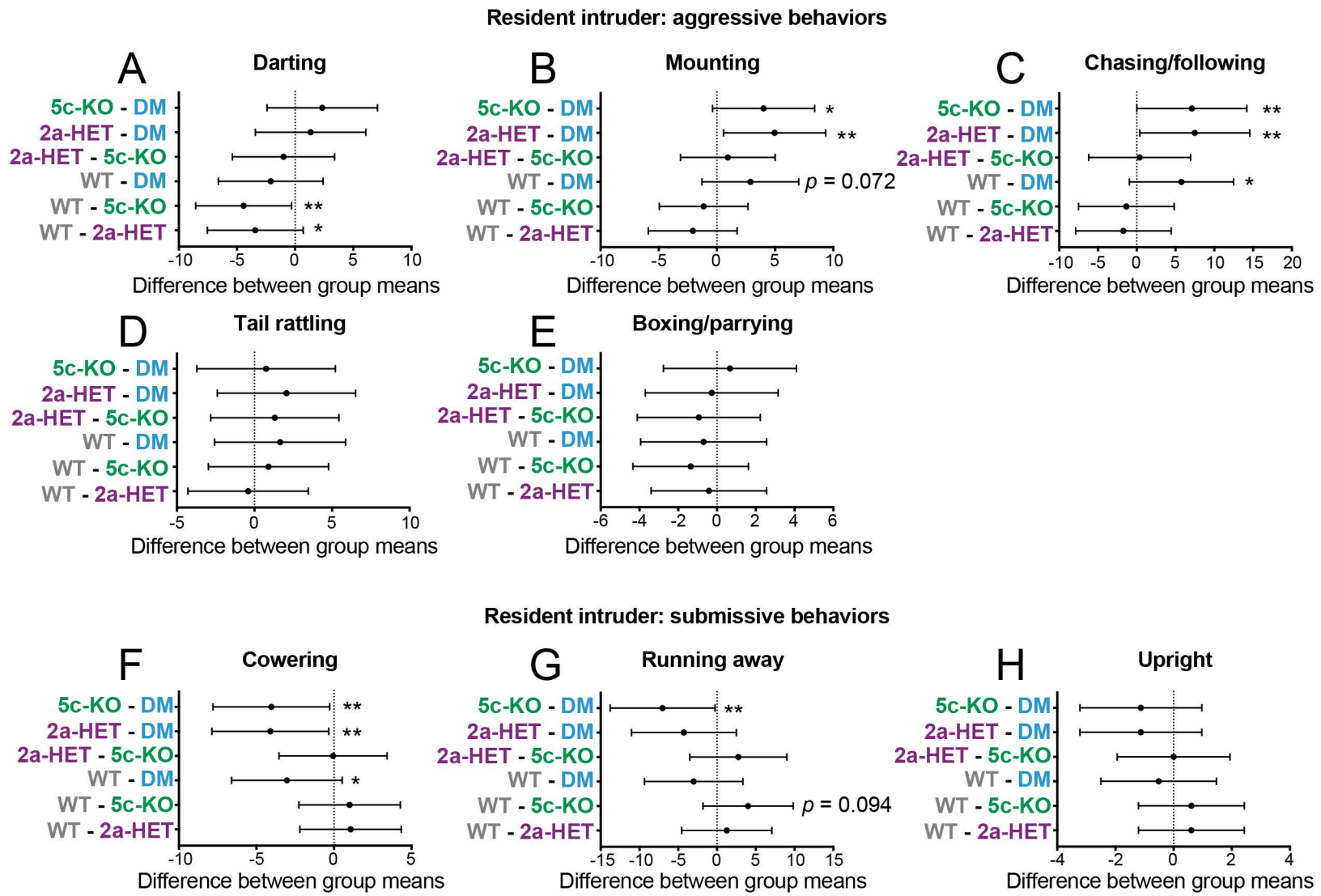

Supplementary Figure 8

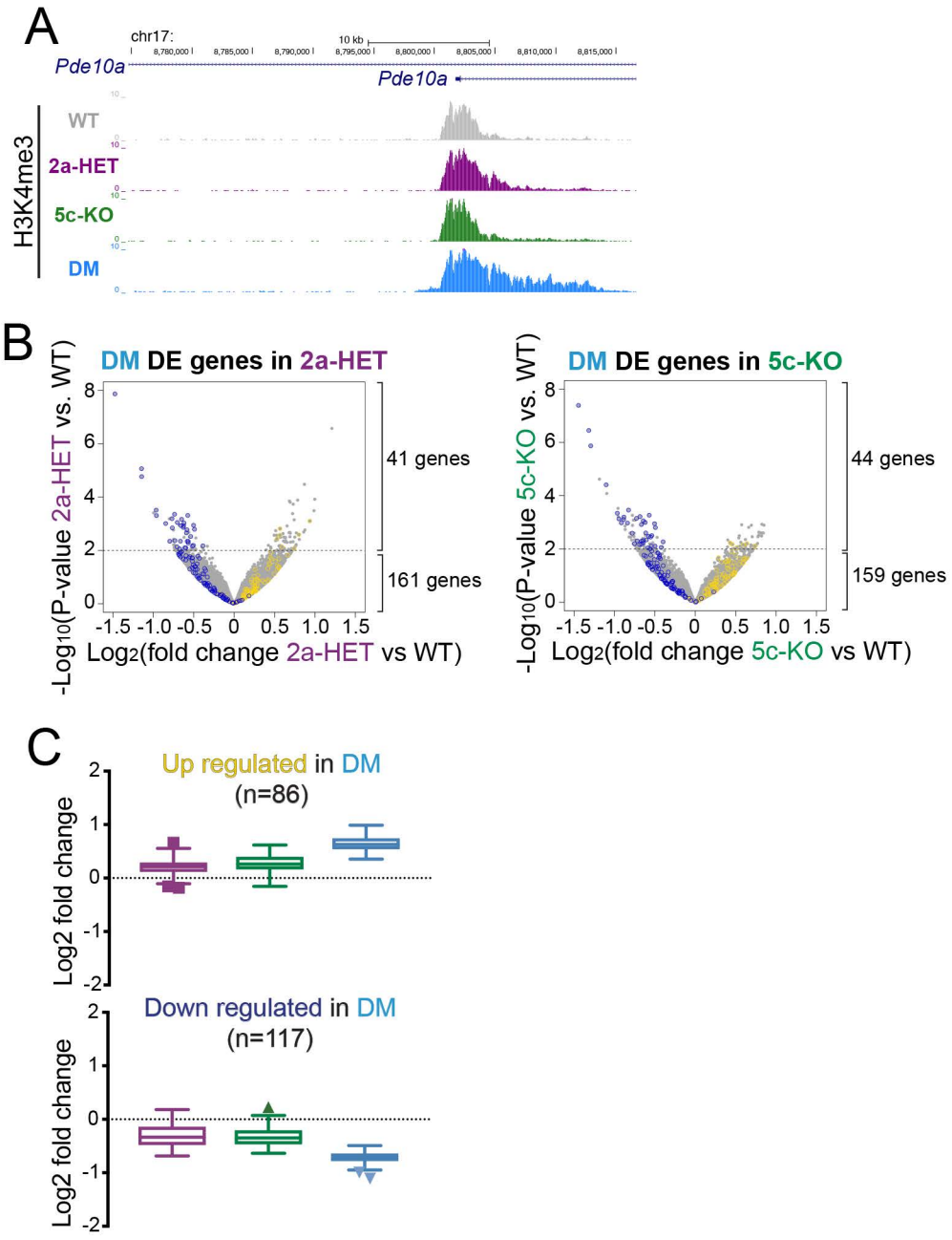

Supplementary Figure 9